The present work was submitted to the Institute of Aerodynamics
and Chair of Fluid Mechanics

Modeling and simulation of deformable Kolmogorov-sized bubbles and droplets in turbulent multiphase flows

Yuhao Tao

Supervisors:
Julian Vorspohl, M.Sc.
Univ.-Prof. Dr.-Ing. Wolfgang Schröder

Aerodynamisches Institut Aachen
RWTH Aachen

A thesis submitted for the degree of
Bachelor of Science Mechanical Engineering

May 2023

Abstract

Bubble/droplet-laden multiphase flows are commonly encountered in industrial applications. While the experimental characterization technique for heavily bubble/droplet-laden flows is immature, and the direct numerical simulation (DNS) is inefficient for heavily Kolmogorov-sized-bubble/droplet-laden systems, the Lagrangian Particle Tracking (LPT) method is utilized to analyze the dynamics of the dispersed phase.

In this work, a two-way coupled Euler-Lagrangian method using a Lattice Boltzmann (LB) solver and the LPT solver is extended. Here, existing point-particle models are used to replace interface-resolving simulations, where empirical force correlations for the motion equation of each dispersed phase individual are adopted. Additionally, based on a phenomenological model proposed by Maffettone and Minale, numerical strategies are developed to describe the temporal evolution of the deformable interface. Additional control loops are designed and implemented to ensure strict volume conservation and preclude the rotation-induced geometrical error, which is caused by the discretization error.

The implemented module is tested in quiescent flow, shear flow, and vortex to validate the implementation and probe the physical mechanisms behind the dispersed phase morphology. In the rising bubble test case, the implementation of the motion equation is validated, and the influences of the coupling between the LB solver and the LPT solver and of the capillary number on the bubble behavior are investigated. Afterward, large-scale simulations of decaying isotropic turbulent flows are carried out to examine the simulation module. The effects of the large-scale existence of the bubble and droplet, their deformability, the density ratio between the dispersed phase and the carrier phase, and the particle size are analyzed. The results may provide insight into the physical mechanisms inside bubble/droplet-laden multiphase flows.

Contents

List of Figures iii

List of Tables vii

Glossary ix

1 Introduction 1

1.1 Motivation 1

1.2 Outline 3

2 Mathematical Model 5

2.1 Correlation network of the multiphase system 5

2.2 Governing equations of fluid motion 6

2.2.1 Incompressible Navier-Stokes equations 6

2.2.2 Kinetic theory and Boltzmann equation 7

2.3 Governing equations of bubble/droplet morphology 8

2.4 Governing equations of bubble/droplet motion 9

3 Numerical Methods 13

3.1 The lattice Boltzmann method 13

3.1.1 Discretization 13

3.1.2 Non-dimensionalization 14

3.2 Bubble/droplet morphology 16

3.2.1 Non-dimensionalization 16

3.2.2 Volume control 16

3.2.3 Correction of rotation-induced geometrical error 17

3.3 Bubble/droplet motion 18

3.4 Algorithms 19

3.4.1 Coupling 19
3.4.2 LPT solution step 19

4 Results 21

4.1 Shape evolution 21
4.1.1 Relaxation 21
4.1.2 Shear flow 24
4.1.3 Vortex 27
4.2 Rising bubble 29
4.2.1 Parameter determination 29
4.2.2 Physical mechanisms 30
4.3 Decaying isotropic turbulence 34
4.3.1 Setup and physical quantities 34
4.3.2 Influence of the density ratio 38
4.3.3 Influence of the capillary number 40
4.3.4 Influence of bubble/droplet diameter 42

5 Summary and Outlook 45

References 47

List of Figures

2.1 The correlation network of the multiphase system 6

3.1 The correlation of relative volume error with interfacial relaxation time $\tau = Ca\tau_\eta$ for initial aspect ratio $d_{31,0} = 2$ and $d_{31,0} = 4$. τ_η for Kolmogorov time scale in LB frame and Ca for capillary number. Relative volume error is the ratio between the volume change of the bubble/droplet and the initial volume. 17

4.1 Quasi-exponential decay of the aspect ratio for a bubble/droplet with $Ca = 0.01, 0.03$, and 0.1. n for simulation time steps and τ_η for Kolmogorov time scale in the LB frame. 22
4.2 Temporal evolution of the time constants τ' during the quasi-exponential decay with $Ca = 0.1$, comparing with the theoretical value. n for simulation time steps and τ_η for Kolmogorov time scale in the LB frame. 23
4.3 Comparison of the average time constants $\bar{\tau'}$ of the quasi-exponential decay, between the calculated values of the semi-major and semi-minor axes of shape function tensor and the theoretical value 23
4.4 Schematic of bubble/droplet deformation in the shear flow, θ for orientation of the bubble/droplet semi-major axis 24
4.5 Correlation of steady orientation of the ellipsoid's semi-major axis in the shear flow with the capillary number, comparison with experimentally validated models and analytical solution 25
4.6 The temporal evolution of the rotation angle of a bubble/droplet with $Ca = 0.5$ under the different intensity of straining α. n for simulation time steps and τ_η for Kolmogorov time scale in the LB frame. 26

4.7 Rotation angle of a rigid bubble/droplet in a vortex. The Kolmogorov time scale τ_η in the LB frame is varied to account for different vorticity. The time step correlates with the time increment in the LPT frame. 28

4.8 Relative bubble/droplet angular velocity to the time step under different vorticity. The Kolmogorov time scale τ_η in the LB frame is varied to account for different vorticity. The time step correlates with a time increment in the LPT frame. 28

4.9 Temporal evolution of the aspect ratio of a rigid bubble/droplet in a vortex. n for simulation time steps and $\tau_\eta = 20$ for Kolmogorov time scale in the LB frame. 28

4.10 Cubic domain for the single rising bubble setup with periodic BC at all domain boundaries 29

4.11 Temporal evolutions of the bubble relative velocity magnitude $|v|/v_T$. The abrupt change of the velocity magnitude of a deformable bubble in the two-way coupled case and the velocity magnitude difference between one-way and two-way coupled cases of rigid bubbles are highlighted. 31

4.12 Temporal evolutions of the bubble relative velocity magnitude $|v|/v_T$ with different capillary numbers Ca. Terminal velocity is evidenced in small Ca cases. 32

4.13 The magnitudes of the acceleration terms in motion equation (Eq. 2.12) relative to the magnitude of the constant buoyancy term on a logarithmic scale for $Ca = 0.1$. The red cross highlights the abrupt change of the lift term. 33

4.14 Temporal evolution of the drag factor C_D, projected area normal to the direction of drag A_D, and bubble aspect ratio d_{31} relative to their respective reasonable initial value after the initial numerical transience, with $Ca = 0.1$ and 10^{-4} 33

4.15 Temporal evolutions of the relative lengths of bubble semi-principal axes to their initial values, and the angle between the semi-principal axes and the velocity difference vector $(\boldsymbol{u} - \boldsymbol{v})$ with $Ca = 0.1$. α and d_3 for semi-major axis, γ and d_1 for semi-minor axis, and β and d_2 for the third semi-principal axis. 34

4.16 Cubic domain for the decaying isotropic turbulence setup with periodic BC at all domain boundaries 35
4.17 Turbulent kinetic energy $E_k(t)$ 39
4.18 Viscous dissipation rate $\varepsilon(t)$ 39
4.19 Spectral distribution of turbulent kinetic energy $\hat{E}_k(\kappa, t)$ 39
4.20 Spectral distribution of viscous dissipation rate $\hat{\varepsilon}(\kappa)$ at $\tilde{t} = 1$ 39
4.21 Kolmogorov length $\eta(t)/\Delta$ 39
4.22 Kinetic energy of the dispersed phase $K(t)$ 39
4.23 Turbulent kinetic energy $E_k(t)$ 41
4.24 Viscous dissipation rate $\varepsilon(t)$ 41
4.25 Spectral distribution of turbulent kinetic energy $\hat{E}_k(\kappa, t)$ 41
4.26 Spectral distribution of viscous dissipation rate $\hat{\varepsilon}(\kappa)$ at $\tilde{t} = 1$ 41
4.27 Kolmogorov length $\eta(t)/\Delta$ 41
4.28 Kinetic energy of the dispersed phase $K(t)$ 41
4.29 Turbulent kinetic energy $E_k(t)$ 43
4.30 Viscous dissipation rate $\varepsilon(t)$ 43
4.31 Spectral distribution of turbulent kinetic energy $\hat{E}_k(\kappa, t)$ 43
4.32 Spectral distribution of viscous dissipation rate $\hat{\varepsilon}(\kappa)$ at $\tilde{t} = 1$ 43
4.33 Kolmogorov length $\eta(t)/\Delta$ 43
4.34 Kinetic energy of the dispersed phase $K(t)$ 43
4.35 Turbulent kinetic energy $E_k(t)$ 44
4.36 Viscous dissipation rate $\varepsilon(t)$ 44
4.37 Spectral distribution of turbulent kinetic energy $\hat{E}_k(\kappa, t)$ 44
4.38 Spectral distribution of viscous dissipation rate $\hat{\varepsilon}(\kappa)$ at $\tilde{t} = 1$ 44
4.39 Kolmogorov length $\eta(t)/\Delta$ 44
4.40 Kinetic energy of the dispersed phase $K(t)$ 44

LIST OF FIGURES

List of Tables

3.1 Non-dimensionalization in the LB frame 15

4.1 Initial parameters for decaying isotropic turbulence setup in the LB units . 35

4.2 Initial parameters for studying the influence of the density ratio ρ_p/ρ_c at particle release time $\tilde{t} = 0.26$ 38

4.3 Initial parameters for studying the influence of the capillary number Ca at particle release time $\tilde{t} = 0.26$ 40

4.4 Initial parameters for studying the influence of bubble/droplet diameter d at particle release time $\tilde{t} = 0.26$ 42

Glossary

Roman Symbols

$\boldsymbol{c}_i$	Discrete velocity vector in lattice Boltzmann space
$\boldsymbol{D}$	Eigenvalue matrix
$\boldsymbol{E}$	Strain rate tensor
$\boldsymbol{F}$	Force vector
$\boldsymbol{f}$	External force per unit mass
$\boldsymbol{g}$	Gravitational acceleration
$\boldsymbol{I}$	Identity matrix
$\boldsymbol{S}$	Shape tensor
$\boldsymbol{u}$	Flow velocity vector
$\boldsymbol{V}$	Eigenvector matrix
$\boldsymbol{v}$	Particle velocity vector
$\boldsymbol{x}$	Vector of Cartesian coordinates
$\hat{T}$	Transfer rate
A_D	Projected area normal to the drag direction
A_L	Projected area normal to the lift direction
C_A	Added mass coefficient
C_D	Drag coefficient
C_L	Lift coefficient
c_s	Speed of sound
d	Number of spatial dimensions, diameter
d_n	Diameter of the projected area
d_{31}	Aspect ratio
e	Euler's number
E_k	Kinetic energy
f	Particle distribution function
f_1	Surface tension prefactor

GLOSSARY

f_2	Stretching prefactor
G	Inverse Kolmogorov turbulent time scale
h	Confinement length scale
II_s	Second invariant
III_s	Third invariant
K	Kinetic energy of dispersed phase
K_1	Coefficient for particle sphericity
K_2	Coefficient for particle sphericity
L	Reference length
L_b	Domain length
N	Number of entities
p	Pressure
R	Universal gas constant, radius
S	Source term, surface area
T	Thermodynamic temperature
t	Time
V	Volume
w	Weight factor

Greek Symbols

α	Angle, intensity of straining
β	Intensity of vorticity
$\boldsymbol{\kappa}$	Wave number vector
$\boldsymbol{\lambda}$	Eigenvalues
$\boldsymbol{\Omega}$	Vorticity rate tensor
$\boldsymbol{\xi}$	Molecular velocity vector
Δ	Difference, grid spacing, discrete quantity
η	Kolmogorov length
$\hat{\mu}$	Viscosity ratio
κ	Wave number
λ	Taylor microscale, eigenvalue
μ	Dynamic viscosity
ν	Kinematic viscosity
Ω	Collision operator
Φ	Arbitrary integral turbulent quantity

ϕ_m	Mass fraction
ϕ_v	Volume fraction
π	Archimedes' constant
Ψ	Kinetic energy transfer rate
ψ	Sphericity
ρ	Density
σ	Interfacial tension
τ	Relaxation time, interfacial relaxation time
τ_η	Kolmogorov time scale
θ	Orientation
ε	Viscous dissipation rate

Superscripts

$'$	Fitted quantity
$*$	Quantity of lattice space, non-dimensional quantity
$-$	Average quantity
$\sim$	Quantity in Lagrange model space
$\wedge$	Quantity in fourier transformed space
eq	Quantity in equilibrium state
T	Transpose

Subscripts

0	Reference value for LBM
∞	Steady state
c	Carrier phase property
i	Index denoting the discretisation in direction of $\boldsymbol{c}_i$, index denoting semi-principal axis of an ellipsoid
n	n-th time step
p	Dipersed phase property
ref	Reference state
rms	Root mean square
T	Terminal value

Dimensionless numbers

Ca	Capillary number
Fr	Froude number
Ma	Mach number
Re	Reynolds number

St	Stokes number
Abbreviations	
BC	Boundary Condition
BGK	Bhatnagar-Gross-Krook (collision operator)
CFD	Computational Fluid Dynamics
DNS	Direct Numerical Simulation
LBM	Lattice Boltzmann Method
LPT	Lagrangian Particle Tracking
m-AIA	Multi-physics PDE solver framework of the Aerodynamic Institue Aachen
NSE	Navier-Stokes equation
ODE	Ordinary Differential Equation
PDE	Partial Differential Equation
PDF	Particle Distribution Function
TKE	Turbulence Kinetic Energy

1

Introduction

1.1 Motivation

Bubble/droplet-laden multiphase flows are commonly encountered in various scientific and industrial scenarios, such as in the design and optimization of bubble column reactors used for gas-liquid reactions in the chemical industry [10, 34], and in wastewater treatment systems, where bubbles are used to transfer oxygen to the water to promote the growth of microorganisms [47]. Additionally, numerical simulations of bubble-laden flows can be used to study underwater bubble plumes and gas dissolution, providing insights into the behavior of bubbles in the ocean, and helping to improve oceanic models [35]. In biomedical engineering, bubble-laden multiphase flow simulations are used to study the behavior of the dispersed phase in elastic blood vessels [54], providing valuable insights for the potential application of drug delivery using microbubbles and ultrasound.

The deformability of dispersed phase in a moving fluid alters the motion pattern of the dispersed phase [7, 11, 12, 21, 22, 32], and in some cases the net momentum or heat transfer in the multiphase system [9, 50, 52], hence may significantly influence the overall behavior of multiphase flows. Given the wide range of applications of multiphase flows, it's of great importance to understand the influence of dispersed phase deformability. However, measurement techniques for characterizing the local flow conditions in heavily bubble/droplet-laden flows are immature. Besides, fully resolved numerical simulations are limited in scale due to the strongly coupled nature between the background flow and dispersed phase, and the complexity of the algorithm [48, 49]. Additionally, such simulations for systems with Kolmogorov-sized bubbles and droplets call for unfeasibly fine grids.

Correspondingly, a numerical simulation of the multiphase flow with the Lagrangian Particle Tracking (LPT) method can be adopted to circumvent these inconveniences [25, 27]. In the LPT method, the dispersed phase is modeled as a collection of Lagrangian particles that are tracked through the flow field. This method allows for a more efficient simulation of multiphase flows because it only requires tracking the Lagrangian particles, rather than fully resolving the phase boundaries between the flow field and the dispersed phase individuals. This significantly reduces the computational cost of the simulation, making it possible to simulate large-scale systems or to perform high-fidelity simulations of complex flows, which has been widely adopted in previous studies of multiphase flow [6, 26, 28, 33, 46, 53, 56]. Moreover, the LPT solver is flexible and can be easily extended to include additional physics, such as the effects of dispersed-phase deformability or chemical reactions between the dispersed and carrier phases. This flexibility allows researchers to model a wide range of multiphase flow problems, making the LPT solver a valuable tool for understanding and optimizing complex flow systems.
The Lattice Boltzmann Method (LBM) is a simulation method commonly used in the field of computational fluid dynamics (CFD) due to its flexibility [5]. It allows for efficient numerical computations and can be easily parallelized to enable large-scale simulations of complex multiphase flows. One of the key advantages of LBM is its ability to handle complex geometries, such as porous media or complex boundaries, without requiring complex mesh generation. Instead, the LBM uses a regular lattice structure and discrete velocity model to simulate the fluid flow, allowing for efficient simulation of complex topologies. Additionally, various point-particle models have been effectively combined with LBM to simulate turbulent convection in a heated channel cavity, as well as particle settling in multifarious setups [19].

In this work, the influence of the deformable Kolmogorov-sized bubbles and droplets on the multiphase flow system is investigated. The in-house flow solver m-AIA is extended, which is a multi-physics PDE solver framework with a focus on fluid dynamics equations. It is developed at the Institute of Aerodynamics of the RWTH Aachen University in Germany. Here, existing point-particle models are used to replace interface-resolving simulations by using empirical force correlations for the motion equation of each dispersed phase individual [45]. Additionally, based on a phenomenological model proposed by Maffettone and Minale [24], numerical strategies are developed to describe the temporal evolution of the deformable interface, which is implemented in the LPT solver. Additional control loops are designed and implemented to account for numerical errors to ensure strict volume conservation and nullify rotation-induced geometrical error.

The implemented module is tested in quiescent flow, shear flow, and vortex to examine the implementation and probe the physical mechanisms behind dispersed phase morphology. Then, the implementation of the motion equation is examined in the case of a laminar rising bubble under gravitation, where the effect of the coupling and the bubble deformability on the process is evidenced. Afterward, large-scale simulations of bubble/droplet-laden isotropic turbulence are carried out and compared with previous and computational results [15] to examine the simulation module. The effects of the large-scale existence of the bubbles and droplets, their deformability, the density ratio between the dispersed phase and the flow field, and the size of the dispersed phase individual are probed.

Overall, the results of this study may provide insights into the behavior of Kolmogorov-sized bubbles and droplets in flow fields, which can be used to improve the design and operation of various industrial and environmental processes. Additionally, the numerical methods developed in this work can be applied to a wide range of multiphase flow problems, providing a versatile tool for future research in this area.

1.2 Outline

The structure of this thesis consists of several chapters. Chapter 2 provides an overview of the fundamental mathematical models that describe the governing equations of both the fluid and dispersed phases. Chapter 3 discusses the numerical method in detail, including the discretization and non-dimensionalization of the LBM, dispersed phase morphology, additional control loops, and the motion equation for deformable bubbles and droplets. In Chapter 4, the conducted simulations are analyzed and compared to corresponding reference data. Specifically, in the rising bubble setup, the temporal evolutions of the bubble velocity magnitude in different coupling schemes and under various bubble deformability are compared to the analytical terminal velocity of the bubble. The temporal evolutions of the dispersed-phase morphological properties, e.g. aspect ratio, steady orientation, and rotation angle, under different flow conditions, such as relaxation, shear flow, and vortex, are demonstrated and compared to available theoretical values. The effects of volume control and geometry correction are evidenced. The results from Direct Numerical Simulations (DNS) of single-phase and bubble/droplet-laden decaying isotropic turbulence are reported. The properties of the flow field, e.g. the Turbulence Kinetic Energy (TKE), viscous dissipation rate, and Kolmogorov length scale, and the properties of the dispersed phase, e.g. the kinetic energy of the dispersed phase, are investigated, considering multiple density ratios between the dispersed phase and the carrier phase, dispersed phase deformability, and size. Finally, Chapter 5 summarizes the obtained results and provides a brief outlook on potential research areas in the future.

2

Mathematical Model

2.1 Correlation network of the multiphase system

The correlation network of the multiphase system is demonstrated in Fig. 2.1, which is a lucid introduction to the mathematical models in this work. The major physical candidates in the process and their ways of communication are interpreted.

In the simulations that this work considers, the flow field, bubble/droplet, and external force are active participants. The dynamics of the flow field itself can be captured by the mathematical models in section 2.2. The bubble/droplet that we investigate has two main features, namely the shape and the position, described by the mathematical models in sections 2.3 and 2.4, respectively. The external force can be gravitational or electromagnetic. Gravity is considered in this work, which influences the bubble/droplet position through the buoyancy effect.

While the bubble/droplet motion is manipulated by the flow field through the drag, the lift, and the added mass forces, the bubble/droplet also gives back a reaction force on the ambient flow field in the two-way coupled case. The bubble/droplet geometry is influenced by the flow field due to the strain and vorticity effects, and by the surface tension, which derives from the shape of the bubble/droplet itself. Although its shape does not have a direct effect on the flow field, it alters the projected area normal to the drag and the lift direction in the drag and the lift terms of the motion equation, so the bubble/droplet motion can be altered due to its deformability. This can indirectly lead to further changes in the flow field due to the reaction force of the dispersed phase on the flow field in the two-way coupled case, which equates to a pseudo-two-way coupling between the bubble/droplet geometry and the flow field.

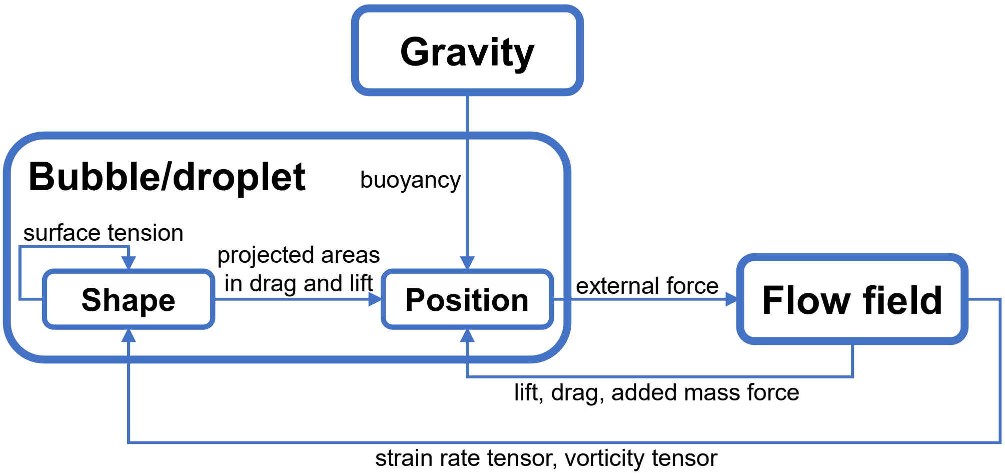
Gravity
Bubble/droplet
buoyancy
surface tension
projected areas
in drag and lift
Shape
Position
external force
Flow field
lift, drag, added mass force
strain rate tensor, vorticity tensor

Figure 2.1: The correlation network of the multiphase system

2.2 Governing equations of fluid motion

2.2.1 Incompressible Navier-Stokes equations

The incompressibility of the flow leads to a solenoidal velocity field with

$$\nabla \cdot \boldsymbol{u} = 0. \tag{2.1}$$

where the variable $\boldsymbol{u}$ is the flow velocity vector [2], which demonstrates the conservation of mass in the incompressible Navier-Stokes equations (NSE). The conservation form of the momentum equation in incompressible NSE reads

$$\frac{\partial \boldsymbol{u}}{\partial t} + (\boldsymbol{u} \cdot \nabla)\boldsymbol{u} = -\frac{1}{\rho}\nabla p + \nu \nabla^2 \boldsymbol{u} + \boldsymbol{f}. \tag{2.2}$$

where p is the pressure, ρ is the fluid density, ν is the fluid viscosity, $\boldsymbol{f}$ is the external force per unit mass, and ∇ is the gradient operator. The equation describes the acceleration of the fluid particles. Its left-hand side represents the time derivative of the velocity vector $\boldsymbol{u}$ and the convective acceleration of the fluid, namely the acceleration due to the motion of the fluid itself. The right-hand side represents the pressure gradient, viscous forces, which results from the friction between adjacent fluid layers, and external forces such as gravity or electromagnetic fields [2].

The assumption of incompressibility precludes the occurrence of density and pressure waves, such as sound or shock waves, rendering this simplification impractical for investigating these phenomena. However, the incompressible flow assumption applies to all fluids at low Mach numbers (e.g. up to approximately Mach 0.3) and is well-suited for modeling air flows under normal temperatures, particularly in the context of atmospheric wind modeling [1].

2.2.2 Kinetic theory and Boltzmann equation

The particle distribution function (PDF) $f(\boldsymbol{\xi}, \boldsymbol{x}, t)$, which is the fundamental variable in kinetic theory, represents the density of the matter in both three-dimensional physical space at the coordinate $\boldsymbol{x}$, in three-dimensional velocity space with the particle velocity $\boldsymbol{\xi}$, and at time point t.

The temporal evolution of $f(\boldsymbol{\xi}, \boldsymbol{x}, t)$ can be described by the Boltzmann equation

$$\frac{\partial f}{\partial t} + \boldsymbol{\xi} \cdot \nabla_x f + \frac{\boldsymbol{F}}{\rho} \cdot \nabla_\xi f = \Omega(f). \tag{2.3}$$

The first two terms on the left-hand side denote the advection of the distribution function by the velocity of its constituent particles $\boldsymbol{\xi}$. The third term describes the effect of external forces (such as gravity or electromagnetic fields) on the distribution function. The source term on the right-hand side is the collision operator, which represents the effects of particle-particle interactions on the distribution function. The collision operators employed in LBM are typically derived from the relatively simpler BGK collision operator (Eq. (2.4)), invented by Bhatnagar, Gross, and Krook [3, 19].

$$\Omega(f) = -\frac{1}{\tau}\left(f - f^{eq}\right) \tag{2.4}$$

The relaxation time τ determines the evolution speed of the distribution function towards the equilibrium distribution f^{eq}, and its value correlates with the transport coefficients such as viscosity and heat diffusivity [19]. The equilibrium distribution f^{eq} reads

$$f^{eq}(\rho, \boldsymbol{u}, T, \boldsymbol{\xi}) = \frac{\rho}{(2\pi RT)^{\frac{d}{2}}} e^{-(\boldsymbol{\xi}-\boldsymbol{u})^2/(2RT)}. \tag{2.5}$$

where ρ is the local density, d is the number of spatial dimensions, R is the universal gas constant, and T is the thermodynamic temperature. The physical meaning is that the microscopic particle-particle interaction constantly drives the system toward equilibrium.

2.3 Governing equations of bubble/droplet morphology

The morphology of the dispersed phase is based on the phenomenological model developed by Maffettone and Minale [24], which was adopted by Spandan et al. [44, 45] and Biferale et al. [4] in their works on deformable microparticles. Under the assumption that the particles are triaxial ellipsoids, the shape and the orientation of the particles can be described by a second-order positive-definite symmetric tensor $\boldsymbol{S}$ (shape tensor). It satisfies the condition $\boldsymbol{S}^{-1} : \boldsymbol{x}\boldsymbol{x} = 1$, where $\boldsymbol{x}$ is the position vector of any point on the ellipsoid surface relative to its center. For any known $\boldsymbol{S}$, the eigenvalues $\boldsymbol{\lambda}$ of the shape tensor give the square of the semiaxes of the ellipsoid while the eigenvectors give the orientation of the semiaxes of the ellipsoid. The shape equation reads

$$\frac{d\boldsymbol{S}}{dt} - (\boldsymbol{\Omega}\boldsymbol{S} - \boldsymbol{S}\boldsymbol{\Omega}) = -\frac{f_1}{\tau}(\boldsymbol{S} - g(\boldsymbol{S})\boldsymbol{I}) + f_2(\boldsymbol{E}\boldsymbol{S} + \boldsymbol{S}\boldsymbol{E}). \tag{2.6}$$

Here $\boldsymbol{\Omega} = 0.5\left[\nabla\boldsymbol{u} - \nabla\boldsymbol{u}^{\mathrm{T}}\right]$ and $\boldsymbol{E} = 0.5\left[\nabla\boldsymbol{u} + \nabla\boldsymbol{u}^{\mathrm{T}}\right]$ represent the vorticity rate and strain rate tensor, respectively. $\boldsymbol{u}$ is the interpolated flow velocity at the particle position. $\tau = \mu_c R/\sigma$ corresponds to the interfacial relaxation time, where μ_c is the dynamic viscosity of the carrier phase, R is the radius of the undeformed particle, and σ is the interfacial tension. Also, the function

$$g(\boldsymbol{S}) = 3\frac{III_s}{II_s} \tag{2.7}$$

is introduced to preserve the particle volume, which was demonstrated by Maffettone and Minale [24]. Here,

$$II_s = \lambda_1\lambda_2 + \lambda_2\lambda_3 + \lambda_3\lambda_1 \tag{2.8}$$

$$III_s = \lambda_1\lambda_2\lambda_3 \tag{2.9}$$

are the second and third invariant of the shape tensor, respectively, where λ_1, λ_2 and λ_3 are the eigenvalues of a 3×3 matrix. f_1 and f_2 are surface tension and stretching prefactors that are chosen to make the model recover linear asymptotic limits for small capillary number Ca (the ratio of the interfacial relaxation time to the characteristic flow time). According to previous studies [4, 24, 30, 31, 44, 51], besides the dependency of the prefactors on the viscosity ratio $\hat{\mu} = \mu_p/\mu_c$ (p for particle and c for carrier), f_2 depends increasingly on Ca with $Ca > 0.3$, and both prefactors become dependent on R/h (R

for undeformed particle radius and h for confinement length scale) when the bubble is relatively large in comparison to the shearing walls i.e. $R/h > 0.15$. Similar to the study of Spandan et al. [45], with $Ca \ll 1$ in this study, the correction of the prefactor which includes an additional dependence of f_2 on Ca is barely necessary. Besides, since only Kolmogorov-sized bubbles and droplets are considered in this case, which corresponds to a locally linearized flow field, the confinement effect appears negligible, so the prefactors f_1 and f_2 barely depend on the confinement length scale. Based on the above arguments, the simplified forms of the prefactors

$$f_1 = \frac{40(\hat{\mu}+1)}{(2\hat{\mu}+3)(19\hat{\mu}+16)} \tag{2.10}$$

$$f_2 = \frac{5}{2\hat{\mu}+3} \tag{2.11}$$

are chosen for this work, where they depend solely on the viscosity ratio $\hat{\mu}$, which is set to 0.01 for bubble-laden flows and set to 100 for droplet-laden flows, in line with previous studies [4, 44, 45].

2.4 Governing equations of bubble/droplet motion

The motion equation of the deformable ellipsoidal bubbles and droplets is based on the formulation of Njobuenwu et al. [33] and Yin et al. [55] for rigid particles, which has been adopted by Spandan et al. in their study of deformable sub-Kolmogorov particles in Taylor Cuoette flow [45]. According to Spandan et al., several conditions are to be fulfilled so that the move function for rigid particles can be applied to the case of deformable bubbles and droplets. Firstly, the bubble/droplet interface is fully contaminated with impurities or surfactants which means a no-slip interfacial boundary condition, similar to that of the rigid particles. Secondly, the characteristic flow time scale is much larger than the interfacial relaxation time scale. Thirdly, the ellipsoidal particles are axisymmetric, which is the case in the work of Njobuenwu et al. [33] and Yin et al. [55]. Under these conditions, the capillary number Ca of the simulation is limited to a maximum of 0.1, and the momentum equation for the dispersed phase can be written as

$$
\begin{aligned}
\rho_p V_p \frac{d\boldsymbol{v}}{dt} =& 0.5\rho_c A_D C_D |\boldsymbol{u}-\boldsymbol{v}|(\boldsymbol{u}-\boldsymbol{v}) + 0.5\rho_c A_L C_L \frac{\boldsymbol{e}_3(\boldsymbol{u}-\boldsymbol{v})}{|\boldsymbol{u}-\boldsymbol{v}|}\left(\boldsymbol{e}_3 \times (\boldsymbol{u}-\boldsymbol{v})\right) \times (\boldsymbol{u}-\boldsymbol{v}) \\
&+ \rho_c V_p C_A \left(\frac{D\boldsymbol{u}}{Dt} - \frac{d\boldsymbol{v}}{dt}\right) + \rho_c V_p \left(\frac{D\boldsymbol{u}}{Dt} - \boldsymbol{g}\right) + \rho_p V_p \boldsymbol{g}.
\end{aligned}
\tag{2.12}
$$

The first term on the right-hand side corresponds to the drag force, the second term corresponds to the lift force, while the last two terms represent the added-mass force and buoyancy, respectively. $\boldsymbol{u}$ and $\boldsymbol{v}$ represent the velocities of the fluid and dispersed phase individual, respectively. $\frac{D}{Dt}$ is the material derivative, $\frac{d}{dt}$ is the derivative along the particle trajectory, $\boldsymbol{e}_3$ is the direction of the ellipsoid's semi-major axis, $\boldsymbol{g}$ is the gravitational acceleration, V_p is the volume of a particle, and the densities of the dispersed phase and the carrier phase are ρ_p and ρ_c, respectively. The drag coefficient C_D in the work of Spandan et al. [45] is founded on the approach developed by Ganser [13], which combines the drag experienced in the Stokes regime (a linear relationship between drag and velocity) and in the Newtonian regime (a quadratic relationship between drag and velocity). The lift coefficient C_L corresponds to the formulation suggested by Hoerner [17], which assumes that the lift is directly proportional to the drag force and is dependent on the relative orientation of the ellipsoid major axis with the slip velocity. The symbols A_D and A_L represent the projected areas normal to the direction of drag and lift, respectively. These values can be computed by the following correlations

$$\frac{C_D}{K_2} = \frac{24}{Re_p K_1 K_2}\left(1 + 0.118\,(Re_p K_1 K_2)^{0.6567}\right) + \frac{0.4305}{1 + \frac{3305}{Re_p K_1 K_2}} \tag{2.13}$$

$$C_L = C_D \sin^2\alpha \cos\alpha \tag{2.14}$$

$$K_1 = \frac{1}{3} d_n/(2R) + \frac{2}{3}\psi^{-0.5} \tag{2.15}$$

$$K_2 = 10^{1.8148(-\log\psi)^{0.5743}} \tag{2.16}$$

$$A_D = \pi R^2 \left(\cos^2\alpha + (4d_{31}/\pi)^2 \sin^2\alpha\right)^{1/2} \tag{2.17}$$

$$A_L = \pi R^2 \left(\sin^2\alpha + (4d_{31}/\pi)^2 \cos^2\alpha\right)^{1/2}. \tag{2.18}$$

$Re_p = 2R|\boldsymbol{u}-\boldsymbol{v}|/\nu$ is the particle Reynolds number calculated based on the initial undistorted radius R of the particle. ν represents the kinematic viscosity of the carrier flow. Coefficients K_1 and K_2 are used to consider the particle sphericity ψ, which represents the ratio of the surface area of a deformed particle to the surface area of an undeformed one. α represents the angle between the largest semi-principal axis and the relative slip velocity ($\boldsymbol{u}$ - $\boldsymbol{v}$), and $d_{31} = d_3/d_1$ represents the ratio between the largest (d_3) and smallest (d_1) semi-principal axis, referred to as the aspect ratio. $d_n = (4A_D/\pi)^{1/2}$ is the diameter of a sphere with the same projection area as that of the deformed particle, A_D.

By computing the added mass coefficient C_A, the formulation of Lai and Mockros for axisymmetric ellipsoidal particles is adopted [20], which depends on the aspect ratio d_{31}. According to Spandan et al. [45], the simplification of the added mass coefficient for a triaxial ellipsoid from a second-order tensor to a fully isotropic coefficient is due to the complex and intractable nature of the given problem. The correlation reads

$$C_A = \frac{d_{31} \ln\left(d_{31} + \sqrt{d_{31}^2 - 1}\right) - \sqrt{d_{31}^2 - 1}}{d_{31}^2 \sqrt{d_{31}^2 - 1} - d_{31} \ln\left(d_{31} + \sqrt{d_{31}^2 - 1}\right)}. \tag{2.19}$$

3

Numerical Methods

3.1 The lattice Boltzmann method

3.1.1 Discretization

In LBM, the distribution function $f(\boldsymbol{\xi}, \boldsymbol{x}, t)$ is discretized in velocity, space and time. The discretization in velocity space is achieved by representing the distribution function using a set of discrete velocity vectors, denoted as $\boldsymbol{c}_i$. These vectors are chosen to be the velocities of particles that propagate on a lattice in discrete time steps.

The distribution function is then approximated by a discrete set of values, $f_i(\boldsymbol{x}, t)$, at the lattice points $\boldsymbol{x}$ and time t. The values of the distribution function $f_i(\boldsymbol{x}, t)$ represent the density of particles with velocity $\boldsymbol{c}_i$ at position $\boldsymbol{x}$ and time t.

The temporal evolution of the distribution function is governed by the discrete Boltzmann equation

$$f_i\left(\boldsymbol{x} + \boldsymbol{c}_i \Delta t, t + \Delta t\right) = f_i(\boldsymbol{x}, t) + \Omega_i(\boldsymbol{x}, t) + S_i. \tag{3.1}$$

where Δt is the time step, S_i is a source term that accounts for the reaction force of the dispersed phase on the flow, and Ω_i is the collision operator, typically based on the BGK approximation

$$\Omega_i(f) = -\frac{f_i - f_i^{eq}}{\tau} \Delta t. \tag{3.2}$$

where τ is the relaxation time, f_i is the discrete distribution function at velocity $\boldsymbol{c}_i$, and f_i^{eq} is the local equilibrium distribution function at velocity $\boldsymbol{c}_i$. The local equilibrium distribution function is given by the Maxwell-Boltzmann distribution and truncated to polynomial form using Hermite expansion, shown in Eq. (3.3).

$$f_i^{eq}(\boldsymbol{x},t) = w_i\rho\left(1 + \frac{\boldsymbol{u}\cdot\boldsymbol{c}_i}{c_s^2} + \frac{(\boldsymbol{u}\cdot\boldsymbol{c}_i)^2}{2c_s^4} - \frac{\boldsymbol{u}\cdot\boldsymbol{u}}{2c_s^2}\right) \tag{3.3}$$

where ρ is the density, $\boldsymbol{u}$ is the macroscopic velocity, w_i is the weight factor, c_s is the speed of sound, and $\cdot$ denotes the dot product. In the implementation, Eq. (3.1) is divided into the collision step and streaming step for more efficient computations (Eq. 3.4, Eq. 3.5). Because the collision step is local and algebraic while the streaming step calls for data on multiple lattice sites [19].

$$f_i^{\star}(\boldsymbol{x},t) = f_i(\boldsymbol{x},t) - \frac{\Delta t}{\tau}\left[f_i(\boldsymbol{x},t) - f_i^{\mathrm{eq}}(\boldsymbol{x},t)\right] \qquad \text{(collision)} \tag{3.4}$$

$$f_i\left(\boldsymbol{x} + \boldsymbol{c}_i\Delta t, t + \Delta t\right) = f_i^{\star}(\boldsymbol{x},t) \qquad \text{(streaming)} \tag{3.5}$$

The density and momentum, as macroscopic moments, are determined from the $finite\ sums$ in the discrete velocity space [19]

$$\begin{aligned} \rho &= \sum_i f_i = \sum_i f_i^{eq} \\ \rho\boldsymbol{u} &= \sum_i f_i\boldsymbol{c}_i = \sum_i f_i^{eq}\boldsymbol{c}_i. \end{aligned} \tag{3.6}$$

With the discretized velocity space, a velocity set as large as necessary and as small as possible should be chosen for the simulation. While D3Q15, D3Q19, and D3Q27 are potential candidates for three-dimensional cases, D3Q15, and D3Q19 are reported to lack rotational invariance for a few non-linear cases, which can jeopardize the simulation of turbulence [19, 43]. Therefore, the D3Q27 velocity set is adopted in this work.

3.1.2 Non-dimensionalization

Non-dimensional variables and parameters are utilized for the calculation, where the reference values are determined as the density ρ_0, the mean thermodynamic velocity ξ_0, the grid distance Δx, and the temperature T_0. Real quantities such as space and time need to be converted to lattice units before simulation. Non-dimensional quantities remain the same. The following non-dimensional variables in Tab. 3.1 are employed in the simulation module.

Variable	Equation
Velocity	$u^* = \frac{u}{\xi_0}$
Isothermal speed of sound	$c_s^* = \frac{c_s}{\xi_0} = \sqrt{\frac{1}{3}}$
Molecular velocity	$\xi_0^* = \frac{\xi_0}{\xi_0} = 1$
Grid distance	$\Delta x^* = \frac{\Delta x}{\Delta x} = 1$
Characteristic Length	$L^* = \frac{L}{\Delta x}$
Time step	$\Delta t^* = \frac{\Delta t \cdot \xi_0}{\Delta x} = 1$
Density	$\rho^* = \frac{\rho}{\rho_0}$
Pressure	$p^* = \frac{p}{\rho_0 \cdot \xi_0^2}$
Collision Operator	$\Omega^* = \omega \cdot \Delta t = \frac{2}{6 \cdot \nu^* + 1}$
Temperature	$T^* = \frac{T}{T_0}$
Thermal diffusivity	$\kappa^* = \frac{\nu^*}{P_r}$
Collision Operator (thermal)	$\Omega_g^* = \omega_g \cdot \Delta t = \frac{2}{6 \cdot \frac{\nu^*}{P_r} + 1}$

Table 3.1: Non-dimensionalization in the LB frame

With the Mach number Ma^* and considering Reynolds similarity

$$Re = \frac{L \cdot u}{\nu} = \frac{L^* \cdot u^*}{\nu^*} = Re^*, \tag{3.7}$$

the non-dimensional kinematic viscosity ν^*, with which the collision operator is calculated, can be computed by,

$$\nu^* = \frac{u^* \cdot L^*}{Re} = \frac{L}{\sqrt{3} \cdot \Delta x} \cdot \frac{Ma^*}{Re}. \tag{3.8}$$

Besides, the Mach number Ma^* is usually utilized to set the physical time step by

$$Ma^* = \frac{u^*}{c_s^*} \Leftrightarrow \Delta t = Ma^* \cdot \frac{\Delta x}{\sqrt{3} \cdot u}. \tag{3.9}$$

Since LBM is based on the kinetic theory that assumes that the fluid is incompressible, Ma^* less than approximately 0.3 is suitable for the simulation. For high Ma^* flows, additional terms can be introduced in the LB equation that accounts for compressibility effects, or the LB solver can cooperate with another solver for high Ma^* by spatial separation of the flow.

3.2 Bubble/droplet morphology

3.2.1 Non-dimensionalization

The shape function is implemented in a non-dimensional form where the dynamics are demonstrated by a control parameter Ca, which is fixed during the simulation, similar to the previous studies [4, 44, 45]. The non-dimensional evolution equation is written as

$$\frac{d\boldsymbol{S}^*}{dt^*} - \left(\boldsymbol{\Omega}^* \boldsymbol{S}^* - \boldsymbol{S}^* \boldsymbol{\Omega}^*\right) = -\frac{f_1}{Ca}\left(\boldsymbol{S}^* - g\left(\boldsymbol{S}^*\right)\boldsymbol{I}\right) + f_2\left(\boldsymbol{E}^* \boldsymbol{S}^* + \boldsymbol{S}^* \boldsymbol{E}^*\right). \tag{3.10}$$

Here, $\boldsymbol{S}^* = \boldsymbol{S}/R^2$ is the non-dimensional shape function, where R is the radius of the undeformed bubble/droplet. $\boldsymbol{\Omega}^* = \boldsymbol{\Omega}/G$ and $\boldsymbol{E}^* = \boldsymbol{E}/G$ are the non-dimensional vorticity rate and strain rate tensors, where $G = 1/\tau_\eta$ is the inverse of the Kolmogorov turbulent time scale in LPT frame. In this work, τ_η is computed based on the two-point correlation [36]. $dt^* = dt/\tau_\eta$ is the non-dimensional time step of the shape function, and $Ca = \tau/\tau_\eta$ is the definition of the capillary number.

3.2.2 Volume control

With the interfacial relaxation time τ reducing to the level of $O(1)$ in the LB frame, it was observed in the relaxation test case that the volume change becomes significant. This test case ignores the flow field and aims to examine the process of an ellipsoidal bubble/droplet gradually recovering into a sphere under the action of surface tension. Since this process is mathematically proved in the work of Maffettone and Minale to conserve the bubble volume [24], the numerical error is considered to harm the integrity of the equation. The predictor-corrector scheme reduces the volume change during relaxation by approximately 1 to 2 orders of magnitude, as shown in Fig. 3.1.

However, significant volume error at the level of 5% still exists for the small τ cases with an initial aspect ratio of 4 and 2, demonstrating the necessity for volume control in these cases. Moreover, since the illustrated data indicate only the volume error production of a single relaxation process, and the large-scale simulations with flow field constantly introduce variations with hardly a steady state, the volume error can potentially accumulate to a large value and harm the integrity of the simulations even for the large τ cases. With the condition of a low Mach number ($Ma < 0.3$) in this work, which corresponds to the incompressible flow, an extra step is introduced to control the bubble volume for each time increment, where the volume is set to the initial value.

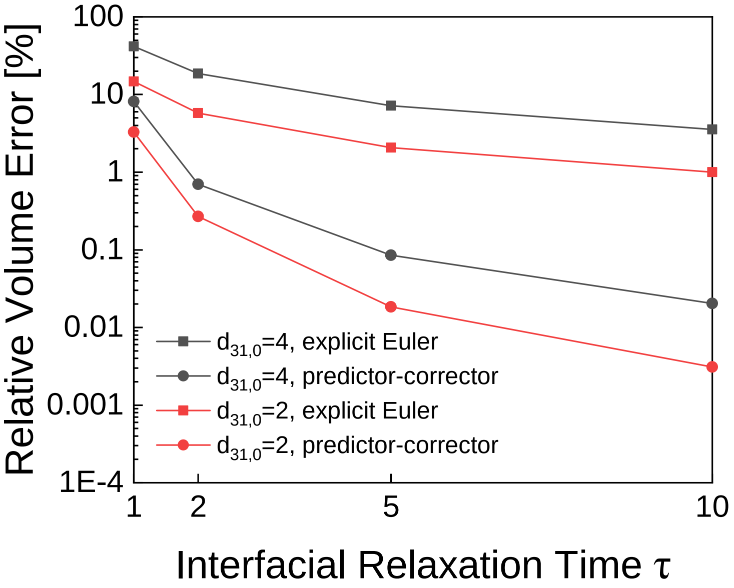

Figure 3.1: The correlation of relative volume error with interfacial relaxation time $\tau = Ca\tau_\eta$ for initial aspect ratio $d_{31,0} = 2$ and $d_{31,0} = 4$. τ_η for Kolmogorov time scale in LB frame and Ca for capillary number. Relative volume error is the ratio between the volume change of the bubble/droplet and the initial volume.

3.2.3 Correction of rotation-induced geometrical error

In the vortex test case with a constant vorticity tensor, and without considering surface tension or strain rate, the ellipsoid is expected to perform the pure rotational motion. However, a stepwise change of the bubble/droplet geometry is observed, and this change converges to zero with a rising Kolmogorov time scale. Hence, this phenomenon is believed to derive from discretization error. This error is observed to demonstrate no dependency on the direction of the rotation and tends to increase the aspect ratio of the bubble.

To pursue the decoupling between shearing and rotating motion, an extra term is added in Eq. (3.10) to compensate for the rotation-induced geometrical error, which is

$$\frac{d\boldsymbol{S}^*}{dt^*}|_{correction} = -\tau_\eta \boldsymbol{V}^*_{n+1}(\boldsymbol{D}^*_{n+1} - \boldsymbol{D}^*_n)\boldsymbol{V}^{*T}_{n+1}, \tag{3.11}$$

$$\boldsymbol{V}^*_{n+1}\boldsymbol{D}^*_{n+1}\boldsymbol{V}^{*T}_{n+1} = \boldsymbol{S}^*_{n+1} = \boldsymbol{S}^*_n + (\boldsymbol{\Omega}^*_n\boldsymbol{S}^*_n - \boldsymbol{S}^*_n\boldsymbol{\Omega}^*_n)dt^*. \tag{3.12}$$

Here, τ_η is the Kolmogorov time scale in LB frame, $\boldsymbol{S}^*_n$ is the shape function of this time step, $\boldsymbol{S}^*_{n+1}$ is the shape function at a virtual next time step that only considers the vorticity term in Eq. (3.10), $\boldsymbol{V}^*_{n+1}$ and $\boldsymbol{D}^*_{n+1}$ are the eigenvector and eigenvalue matrices of $\boldsymbol{S}^*_{n+1}$,

respectively, and T denotes the transpose of a matrix. This term sets to zero the shape change caused by the vorticity for every time step.
Besides, it is observed that the correction term introduces a shift of steady orientation in the shear flow test case. As a result, this term is deactivated when

$$\frac{\|\boldsymbol{S}_n^* - \boldsymbol{S}_{n-1}^*\|_F}{dt^*} \leq 0.01, \tag{3.13}$$

which indicates the proximity of the steady state. $\|\cdot\|_F$ represents the Frobenius norm.

3.3 Bubble/droplet motion

Since a large density ratio between the dispersed phase and the flow field leads to instability in the numerical solution of the motion equation Eq. (2.12), the move function is transformed so that the influence of the density ratio is minimized, which is written as

$$\begin{aligned}\frac{d\boldsymbol{v}}{dt} =& \frac{\rho A_D C_D}{2(\rho_p + \rho C_A)V_p}|\boldsymbol{u}-\boldsymbol{v}|(\boldsymbol{u}-\boldsymbol{v}) + \frac{\rho A_L C_L}{2(\rho_p + \rho C_A)V_p}\frac{\boldsymbol{e}_3(\boldsymbol{u}-\boldsymbol{v})}{|\boldsymbol{u}-\boldsymbol{v}|}(\boldsymbol{e}_3 \times (\boldsymbol{u}-\boldsymbol{v})) \times (\boldsymbol{u}-\boldsymbol{v}) \\ &+ \frac{\rho(C_A+1)}{\rho_p + \rho C_A}\frac{D\boldsymbol{u}}{Dt} + \frac{\rho_p - \rho}{\rho_p + \rho C_A}\boldsymbol{g}.\end{aligned} \tag{3.14}$$

In the calculation of the sphericity ψ for the drag coefficient in the motion equation, the surface area of an ellipsoid is necessary, where a precise solution is not available. Knud Thomsen's Formula is then utilized to approximate the surface area value, which yields a relative error of at most 1.061%. The formula reads

$$S = 4\pi\sqrt[p]{\frac{a^p b^p + a^p c^p + b^p c^p}{3}}, \ p = 1.6075. \tag{3.15}$$

Here S represents the ellipsoid surface area, and a, b, and c, are the lengths of the three semiaxes.
Besides, the denominator of Eq. (2.19) for the added mass coefficient C_A in the motion equation becomes zero when the bubble/droplet is purely spherical, which cripples the numerical solution. Since $C_A = 0.5$ for perfect spheres [8], the coefficient is set to 0.5 in the implemented module when $d_{31} < 1 + 10^{-6}$. This is in accordance with Eq. (2.19), where $C_A(d_{31} = 1 + 10^{-6}) \approx 0.499994$.

3.4 Algorithms

3.4.1 Coupling

In the case where the motion of the dispersed phase and the flow field are one-way coupled, the forces that the fluid exerts on the dispersed phase are considered and the effect of the reaction force of the dispersed phase on the local flow field is ignored. As a result, in the case where the flow field is initially quiescent, namely the rising bubble test case in section 4.2, no geometrical change in the bubble can occur. This means that the bubble geometry is decoupled from the flow field for a one-way coupling between the bubble motion and the fluid. The inclusion of the reaction force of particles on the surrounding flow field, following Newton's third law of motion, is known as the two-way coupling of the bubble motion. This is represented by the source term in Eq. (3.1). In this case, the interaction between the bubble and the flow field, as shown in Fig. 2.1 is enabled, which is appropriate for this study.

3.4.2 LPT solution step

The solution step in the LPT solver for the deformable bubbles/droplets can be divided into seven parts. Firstly, the motion equation with stable form (Eq. (3.14)) is solved using the predictor-corrector scheme when the capillary number $Ca \leq 0.1$, which yields data of particle position, velocity, and acceleration. The morphological change of the particle is then preliminarily determined by the non-dimensional shape function (Eq. (3.10)) in the predictor-corrector scheme. Next, the rotation-induced shape error is calculated and compensated. Afterward, the particle volume is set to the initial value, and the data of the shape function is generated. Then, particle exchange between the domains takes place. The redistribution weights are calculated. Finally, the reaction force of the particle on the fluid is determined in the two-way coupled case.

4

Results

4.1 Shape evolution

4.1.1 Relaxation

In the relaxation test case for the shape function, the temporal evolution of a single bubble/droplet with initial aspect ratio $d_{31,0} = 4$ is investigated, which is influenced only by surface tension under a constant Kolmogorov time scale τ_η of 1000 in LB frame. The strain rate and vorticity tensor in Eq. (3.10) are set to zero, and the capillary number $Ca = 0.01, 0.03$, and 0.1 are chosen for the test case, which is in the range of interest. The motion equation is turned off.

The simulation reproduces the characteristic behavior of a deformed bubble/droplet recovering to the spherical form under the influence of surface tension. In Fig. 4.1, the quasi-exponential decay of the aspect ratio to 1 can be observed, and a smaller Ca increases the rate of the decay. This is reasonable because of the $Ca = \tau/\tau_\eta$. With constant τ_η, smaller Ca corresponds to smaller interfacial relaxation time τ, which represents a quicker recovery of the bubble/droplet to the spherical form.

Since the shearing and rotational influences are neglected for this test case, the ordinary differential equation Eq. (3.10) can be simplified to

$$\frac{d\boldsymbol{S}^*}{dt^*} = -\frac{f_1}{Ca}\left(\boldsymbol{S}^* - g\left(\boldsymbol{S}^*\right)\boldsymbol{I}\right), \tag{4.1}$$

where Ca/f_1 serves as the theoretical time constant $\tau'_{theoretical}$ of the exponential decay for Fig. 4.2 and Fig. 4.3. In the relaxation case, the shape function matrix maintains a diagonal form, and the three diagonal values represent the eigenvalues of the matrix, which correlate with the length of the three semi-principal axes. Their respective time

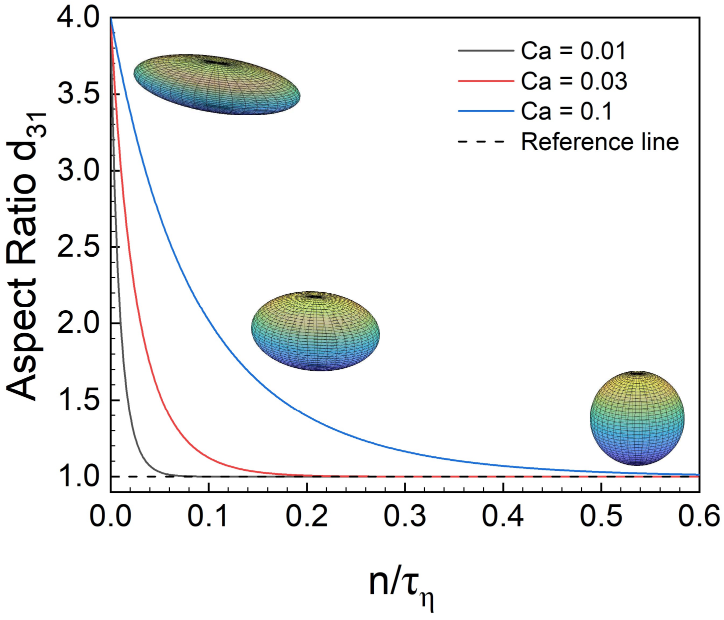

Figure 4.1: Quasi-exponential decay of the aspect ratio for a bubble/droplet with $Ca = 0.01, 0.03$, and 0.1. n for simulation time steps and τ_η for Kolmogorov time scale in the LB frame.

constant τ' in 4.2 for exponential decay can be calculated with the simulation output of the shape function according to

$$\tau_i' = \frac{1 - \lambda_{i,n}}{\lambda_{i,n+1} - \lambda_{i,n}} \Delta t, \tag{4.2}$$

where $\lambda_{i,n}$ is an eigenvalue of shape matrix at this time step, $\lambda_{i,n+1}$ is an eigenvalue at the next time step and $\Delta t = 1/\tau_\eta$ is the time increment, τ_η for Kolmogorov time scale in the LB frame. As demonstrated in Fig. 4.2, τ' is not temporally constant either for the semi-major or the semi-minor axis, which is due to the volume conservation function $g\left(\boldsymbol{S}^*\right)$. The function is observed to rise from a positive value larger than the initial length of the semi-minor axis to 1 during the relaxation, which indicates a changing steady state of Eq. (4.1). Hence, the process behavior deviates greatly from purely exponential. Since $g\left(\boldsymbol{S}^*\right) < 1$, the decay of the semi-major axis appears quicker than the exponential case, because the mathematical steady-state $g\left(\boldsymbol{S}^*\right)$ is farther than 1, corresponding to a smaller time constant τ' than the theoretical value $\tau'_{theoretical}$. On the contrary, the growth of the semi-minor axis is slower than the exponential case, because the mathematical steady state is closer than 1, corresponding to larger τ' than $\tau'_{theoretical}$, matching the results in

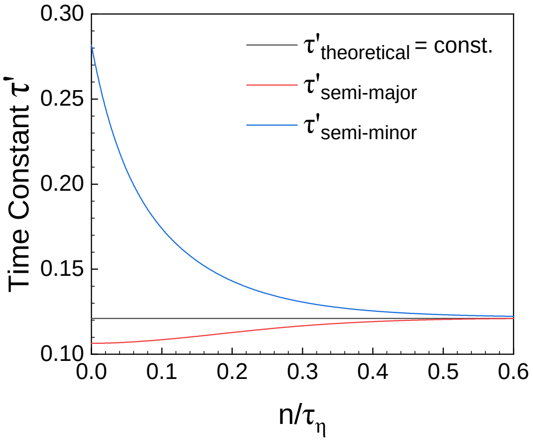

Figure 4.2: Temporal evolution of the time constants τ' during the quasi-exponential decay with $Ca = 0.1$, comparing with the theoretical value. n for simulation time steps and τ_η for Kolmogorov time scale in the LB frame.

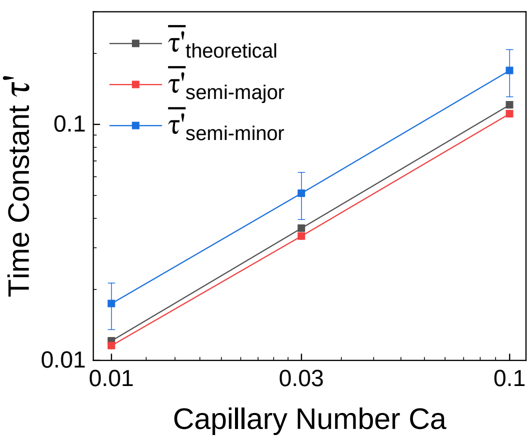

Figure 4.3: Comparison of the average time constants $\bar{\tau}'$ of the quasi-exponential decay, between the calculated values of the semi-major and semi-minor axes of shape function tensor and the theoretical value

Fig. 4.2.

Besides, it was observed that the function $g(\boldsymbol{S}^*)$ approximates 1 and achieves a value above 0.99 after the simulation time of 3τ, where the behavior of ODE becomes nearly exponential. This corresponds to the trend of convergence of $\tau'_{semi-major}$ and $\tau'_{semi-minor}$ to $\tau'_{theoretical}$ in Fig. 4.2. To characterize the non-exponential nature of Eq. (4.1), the average time constants $\bar{\tau}'$ before 3τ and their standard deviations are calculated for the cases with $Ca = 0.01, 0.03$, and 0.1, illustrated in Fig. 4.3. The average time constants are in a linear correlation with Ca, in line with $\tau'_{theoretical} = Ca/f_1$. And the results of the semi-major axis, the theoretical value, and that of the semi-minor axis range from small to large for the same Ca, in line with the deduction in the last paragraph.

The correction of rotation-induced geometrical error hibernates as no vorticity is present, and the forced volume control thoroughly nullifies the volume change due to discretization error. The effect of the volume control on the bubble dynamics is negligible, as it is about four orders of magnitude smaller than the effect of changing the integration strategy from a simple Euler to a predictor-corrector scheme.

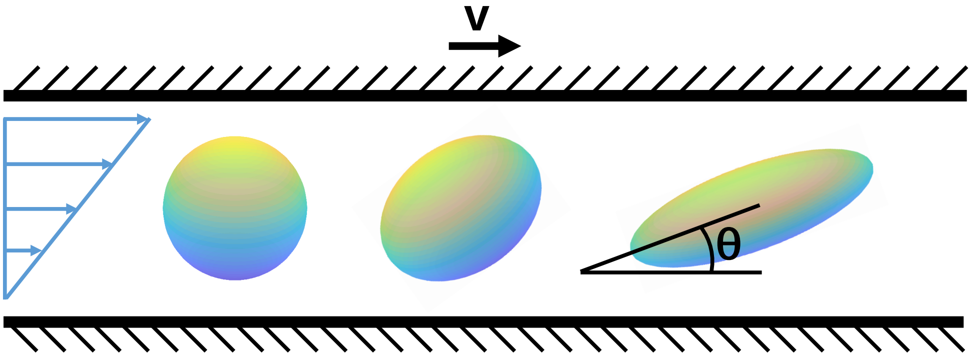

Figure 4.4: Schematic of bubble/droplet deformation in the shear flow, θ for orientation of the bubble/droplet semi-major axis

4.1.2 Shear flow

In the test case for the shear flow, a similar configuration to the work of Maffettone and Minale is employed [24]. The motion equation is turned off. The surface tension term is enabled, and the strain rate tensor $\boldsymbol{E}^*$ and vorticity rate tensor $\boldsymbol{\Omega}^*$ in Eq. (3.10) are set to constant values of

$$\boldsymbol{E}^* = \frac{1}{2}\begin{pmatrix} 0 & 1 & 0 \\ 1 & 0 & 0 \\ 0 & 0 & 0 \end{pmatrix}, \quad \boldsymbol{\Omega}^* = \frac{1}{2}\begin{pmatrix} 0 & 1 & 0 \\ -1 & 0 & 0 \\ 0 & 0 & 0 \end{pmatrix}. \tag{4.3}$$

The test case simulates an initially spherical bubble/droplet, which is deformed in the shear channel, as shown in the schematic in Fig. 4.4. The capillary number Ca is set from 10^{-6} to 0.6 to validate the dynamics of the shape function by comparing it with the analytical solution [24] and experimentally validated models [16, 37, 39]. The Kolmogorov time scale is set constant and tuned according to Ca to make sure the interfacial relaxation can be resolved.

All the test cases with interfacial relaxation time $\tau > 1$ exhibit a steady state, where the particle orientation θ and aspect ratio d_{31} are a perfect match with the theoretical values [24],

$$d_{31,\infty} = \sqrt{\frac{f_1^2 + Ca^2 + f_2 Ca\sqrt{f_1^2 + Ca^2}}{f_1^2 + Ca^2 - f_2 Ca\sqrt{f_1^2 + Ca^2}}}, \tag{4.4}$$

$$\theta_\infty = \frac{1}{2}\arctan\left(\frac{f_1}{Ca}\right) \tag{4.5}$$

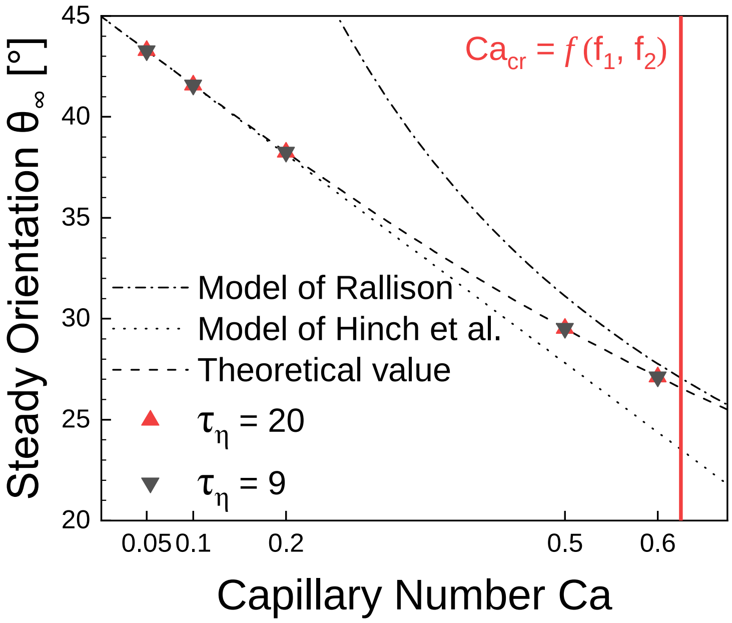

Figure 4.5: Correlation of steady orientation of the ellipsoid's semi-major axis in the shear flow with the capillary number, comparison with experimentally validated models and analytical solution

which justifies the implementation within the mentioned parameter range. Physically, the steady states of θ and d_{31} are both standoffs of forces. As the strain rate tensor tends to shear the ellipsoid into more and more slender form, the relaxation term pulls it back to a sphere due to the surface tension, where $d_{31,\infty}$ comes to exist. While the vorticity tensor tends to rotate the ellipsoid, the strain rate tensor seeks to fix the ellipsoid's orientation at 45 degrees, and the two forces reach a balance point at θ_∞.

In Fig. 4.5, θ_∞ in $Ca \geq 0.05$ cases are compared with the theoretical value [24], model of Hinch et al. [16, 39] for small Ca and model of Rallison [37, 39] for large Ca. The steady-state values are in perfect match with the theoretical calculation regardless of the variation of Kolmogorov time scale τ_η, which represents the variation of the solution time step. In $Ca < 0.5$ cases, the model yields results in line with the prediction of Hinch et al., while $Ca \geq 0.5$ cases better match Rallison's model. Besides, a critical capillary number according to Maffettone and Minale [24]

$$Ca_{cr} = \frac{f_1}{\sqrt{f_2^2 - 1}} \tag{4.6}$$

corresponds to the drop rupture, which is also reproduced in the simulation and indicated

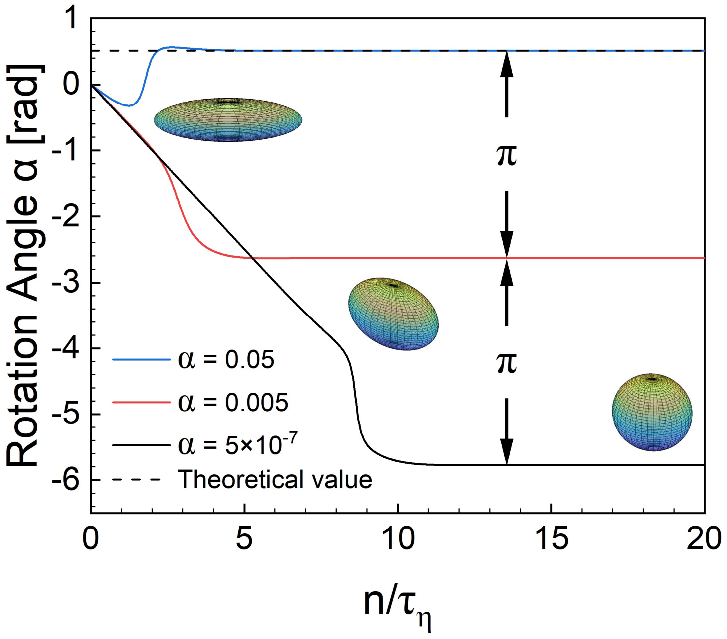

Figure 4.6: The temporal evolution of the rotation angle of a bubble/droplet with $Ca = 0.5$ under the different intensity of straining α. n for simulation time steps and τ_η for Kolmogorov time scale in the LB frame.

by the red line in Fig. 4.5.

For more general cases, the strain rate tensor, and the vorticity rate tensor read

$$\boldsymbol{E}^* = \begin{pmatrix} 0 & \alpha & 0 \\ \alpha & 0 & 0 \\ 0 & 0 & 0 \end{pmatrix}, \quad \boldsymbol{\Omega}^* = \begin{pmatrix} 0 & \beta & 0 \\ -\beta & 0 & 0 \\ 0 & 0 & 0 \end{pmatrix}. \tag{4.7}$$

where α and β can be understood as the intensity of straining and vorticity, respectively. The steady-state formulas in Eq. (4.4) and Eq. (4.5) can be extended to

$$d_{31,\infty} = \sqrt{\frac{f_1^2/Ca^2 + 4\beta^2 + 2\alpha f_2\sqrt{f_1^2/Ca^2 + 4\beta^2}}{f_1^2/Ca^2 + 4\beta^2 - 2\alpha f_2\sqrt{f_1^2/Ca^2 + 4\beta^2}}}, \tag{4.8}$$

$$\theta_\infty = \frac{1}{2}\arctan\left(\frac{f_1}{2\beta Ca}\right). \tag{4.9}$$

With these correlations, the transition from pure particle rotation to being trapped by the steady-state point can be studied. The initial aspect ratio $d_{31,0}$ is set to 4, β is fixed to 0.5, τ_η in LB frame is set to 100, and α is varied at a range close to zero. It's indicated in Fig. 4.6 that the ellipsoid demonstrates linear rotational behavior at the initial stage in all three cases. This is because the ellipsoid's aspect ratio d_{31} at the initial transience is so large, that the vorticity term dominates the ellipsoid's motion. With decreasing d_{31} due to the surface tension term, the ellipsoid deviates more and more from the linear rotational behavior and tends to be attracted by a local steady state. Near the steady state, an acceleration toward the value is observed, where the straining term is considered to be dominant. The final steady state is a balance between the three forces, namely straining, rotating, and surface tension. The straining force pulls the ellipsoid's orientation to $\pi/4$ and tends to increase d_{31} to an infinite value, which is compensated by the rotating force, which tries to rotate the ellipsoid further, and surface tension force, which keeps reducing d_{31} to 1, respectively. The calculated theoretical value with Eq. (4.9) matches the simulation employing $\alpha = 0.05$. It is marked in Fig. 4.6 that the steady-state values have the period of π, which is reasonable considering the axisymmetry of the ellipsoid.

4.1.3 Vortex

The test case for the vortex reproduces the rotational bubble/droplet motion without deformation. The initial particle aspect ratio $d_{31,0}$ is set to 4, the Kolmogorov time scale in LB frame τ_η is varied from 20 to 100, the surface tension is turned off, the strain rate tensor $\boldsymbol{E}^*$ in Eq. (3.10) is set to zero, and the vorticity rate tensor $\boldsymbol{\Omega}^*$ is set to a constant value of

$$\boldsymbol{\Omega}^* = \frac{1}{2}\begin{pmatrix} 0 & 1 & 0 \\ -1 & 0 & 0 \\ 0 & 0 & 0 \end{pmatrix}. \tag{4.10}$$

As demonstrated in Fig. 4.7 and Fig. 4.8, linear rotational motion is observed, reflecting the constant vorticity rate tensor. The angular velocity relative to the time step is inverse linear correlated with τ_η, the Kolmogorov time scale in the LB frame. This is because the time step of the shape function in the LPT solver is $1/\tau_\eta$, which aims at depicting the fact that a more violent flow field yields smaller τ_η so that the temporal evolution of the bubble geometry in LPT frame is correspondingly quicker. Moreover, the rotation-induced geometrical error, which leads to the change of the bubble aspect ratio during pure rotation, is observed to be nullified with the introduced additional term in Eq. (3.12), demonstrated in Fig. 4.9.

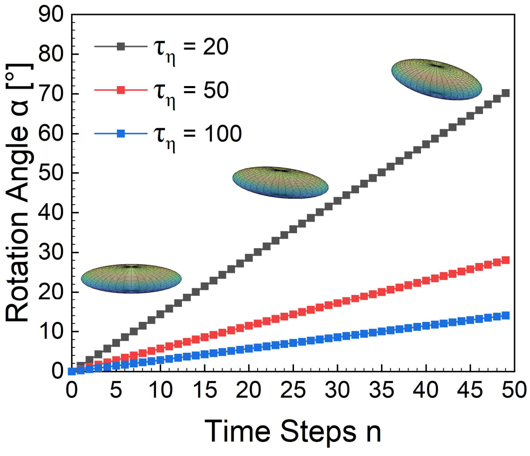

Figure 4.7: Rotation angle of a rigid bubble/droplet in a vortex. The Kolmogorov time scale τ_η in the LB frame is varied to account for different vorticity. The time step correlates with the time increment in the LPT frame.

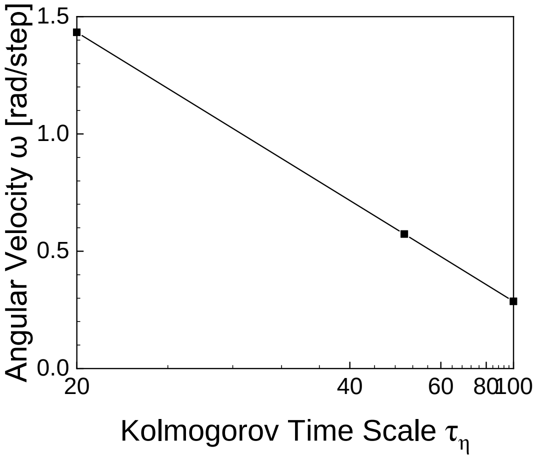

Figure 4.8: Relative bubble/droplet angular velocity to the time step under different vorticity. The Kolmogorov time scale τ_η in the LB frame is varied to account for different vorticity. The time step correlates with a time increment in the LPT frame.

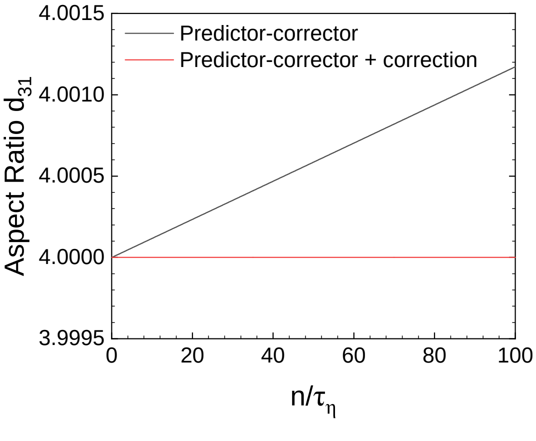

Figure 4.9: Temporal evolution of the aspect ratio of a rigid bubble/droplet in a vortex. n for simulation time steps and $\tau_\eta = 20$ for Kolmogorov time scale in the LB frame.

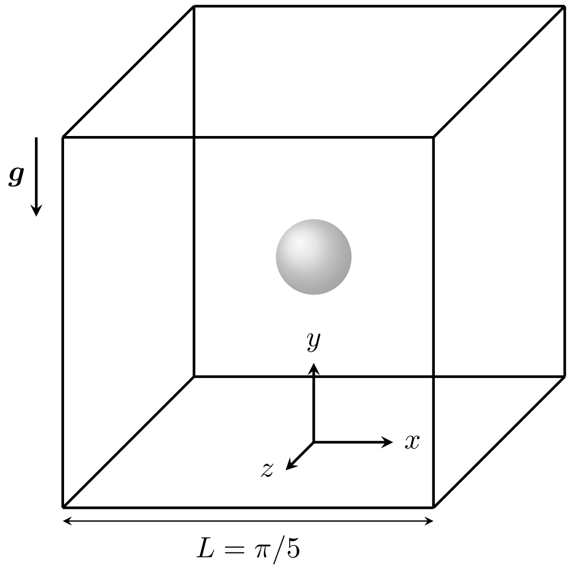

Figure 4.10: Cubic domain for the single rising bubble setup with periodic BC at all domain boundaries

4.2 Rising bubble

The simulation of a single rising bubble is conducted to validate the implementation of the motion equation Eq. (2.12) and investigate the influence of the bubble deformability on this process. A cubic simulation box with the side length of $\pi/5$ m and periodic boundary condition is chosen. An initially spherical bubble with a diameter $d_p = 2 \cdot 10^{-3}$ m is set free from $\boldsymbol{x}(t = 0) = (0, 0, 0)^T m$ and moves in the flow field under the gravitational acceleration of $\boldsymbol{g} = (0, -9.81, 0)^T m/s^2$. The initial configuration is showcased in Fig. 4.10. The density of the fluid is 1000 kg/m^3 and the density of the bubble is 1 kg/m^3, similar to the density of air. The kinematic viscosity ν of the fluid is set to 10^{-6} m^2/s. A uniform refinement of level 7 is applied, corresponding $2^7 = 128$ cells in each direction.

4.2.1 Parameter determination

While $Ma^* = 0.1$ and $Ca \in [0, 0.1]$ are adopted, Re and Fr are chosen according to the terminal velocity of the bubble, which can be analytically determined. Under the assumption that drag and buoyancy are the dominant influences on the bubble motion, which is demonstrated in Fig. 4.13, Eq. 2.12 can be simplified to

$$0.5\rho_c A_D C_D |\boldsymbol{u} - \boldsymbol{v}|(\boldsymbol{u} - \boldsymbol{v}) = (\rho_c - \rho_p) V_p \boldsymbol{g} \tag{4.11}$$

at the steady state. Moreover, the bubble in similar test cases hardly agitated the flow field. It is hence further assumed that the flow velocity is negligible and the direction of the bubble velocity is approximately on the contrary of the gravity. The terminal velocity v_T then has the form

$$v_T = \sqrt{\frac{2(\rho_c - \rho_p) V_p g}{\rho_c A_D C_D}}. \tag{4.12}$$

With negligible flow field, the shape function of the bubble (Eq. (2.6)) is barely triggered, so that the bubble deformation is considered to be trivial, which leads to another assumption that the bubble maintains a spherical form during the process, namely $d_{31} = \psi = K_2 = 1$ for the motion equation Eq. (2.12) and its sub-equations. Without the dependency on the aspect ratio d_{31}, the projected area $A_D(\alpha)$ vibrates in a small interval of $[\pi R^2, 4R^2]$ with a periode of π. Considering $A_D = 4R^2$, the coefficient $K_1 = 2/(3\sqrt{\pi}) + 2/3$. With $Re_p = d_p v_T/\nu = 2000 v_T$, the drag factor

$$C_D(v_T) = \frac{1 + 0.118(2085.586 v_T)^{0.6567}}{86.8994 v_T} + \frac{0.4305}{1 + \frac{1.584686}{v_T}}. \tag{4.13}$$

Substituting the values into Eq. (4.12), then the formula becomes $v_T = f(v_T)$, and yields the result of $v_T = 0.21248 m/s$. The Re_p and Fr_p for this simulation are consequently 424.96 and 1.517, respectively.

4.2.2 Physical mechanisms

In Fig. 4.11, the temporal evolution of the bubble velocity magnitude is compared with the analytical terminal velocity, and the results with one-way and two-way coupling are juxtaposed. The simulation result is generally a good match with the analytical solution. The two-way coupling itself is observed to slightly enhance the bubble velocity, shown by the blue line, which is in line with the previous result [15]. It is because the motion of a spherical particle is less impeded in a mobile flow field, namely the two-way coupled case, where the moving fluid with the bubble leads to a smaller velocity difference between the particle and the fluid, hence lower drag. However, the velocity increase is one to two orders

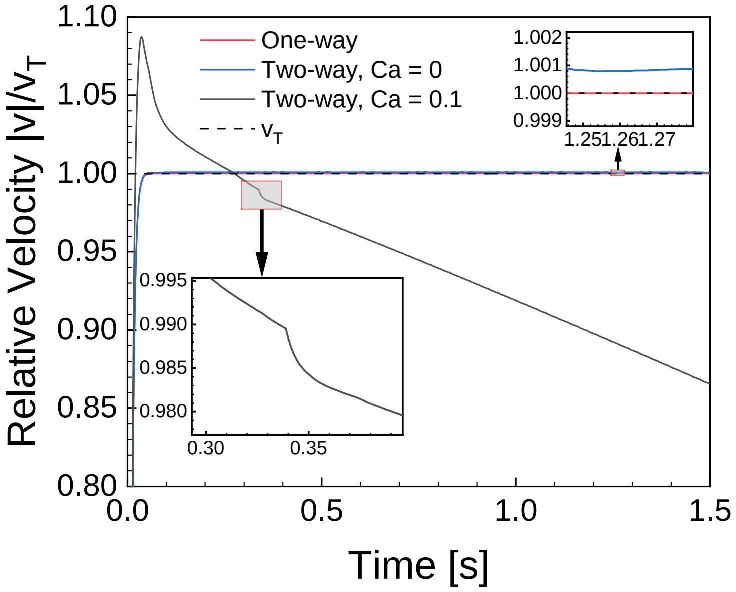

Figure 4.11: Temporal evolutions of the bubble relative velocity magnitude $|v|/v_T$. The abrupt change of the velocity magnitude of a deformable bubble in the two-way coupled case and the velocity magnitude difference between one-way and two-way coupled cases of rigid bubbles are highlighted.

of magnitude smaller than the previous result [15]. This is because the particle density is 2560 times smaller than in their case, so the momentum transport to the fluid due to the bubble motion is much weaker, causing a much less agitated flow field.

In Fig. 4.12, an upsurge of the bubble velocity magnitude is noticed before 0.05 seconds. The relatively high levels of lift term and added mass term at this stage are considered to contribute to this phenomenon according to Fig. 4.13. Moreover, the bubble velocities in the two-way coupled cases are observed to decrease until a certain steady value, which can be lower than the analytical terminal velocity, demonstrated in Fig. 4.12. This velocity decline is considered to be the joint effort of the bubble deformation and rotation, consequently increasing the drag effect. Besides, a sudden acceleration of the bubble can be observed at approximately 0.34 seconds, highlighted in Fig. 4.11. The reason is the switch of the bubble semi-major axis, which can be visualized by the data in Fig. 4.15. Consequently, the lift term is reduced to zero because the new semi-major axis is observed to be perpendicular to the velocity difference vector $(\boldsymbol{u} - \boldsymbol{v})$ between the flow field and the bubble, demonstrated in Fig. 4.13. As shown in Fig. 4.12, the larger the capillary number Ca, the longer the process of velocity decrease. The case with $Ca = 0.1$ is further

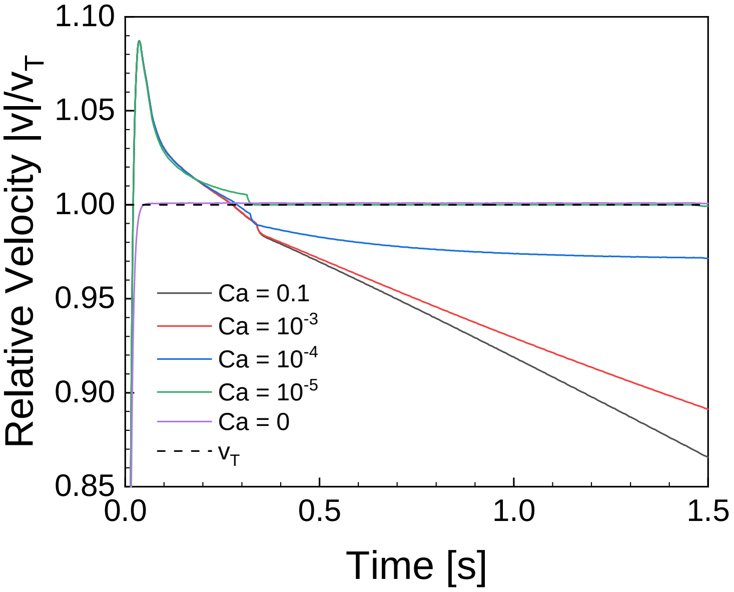

Figure 4.12: Temporal evolutions of the bubble relative velocity magnitude $|v|/v_T$ with different capillary numbers Ca. Terminal velocity is evidenced in small Ca cases.

probed to better understand this transient state.

In Fig. 4.13, the magnitude of the temporal evolution of drag, lift, added mass, and buoyancy terms are juxtaposed on a logarithmic scale. The drag and buoyancy are dominant after 0.05 seconds, which may justify the assumption drawn for calculating the bubble terminal velocity. The lift term decreases steadily after the initial transience with the bubble semi-major axis rotating towards the direction perpendicular to the velocity difference $(\boldsymbol{u}-\boldsymbol{v})$, until the sudden change of the bubble semi-major axis.

In Fig. 4.14, the evolutions of three drag-related factors, namely the projected area A_D, drag factor C_D, and bubble aspect ratio d_{31} in the two-way coupled case are demonstrated. The bubble-induced flow field causes the bubble geometry to deviate from the perfect sphere. The increase of A_D and C_D contributes directly to the drag in Eq. (2.12), reducing the velocity difference $(\boldsymbol{u}-\boldsymbol{v})$ to compensate the constant buoyancy term, hence indirectly lowers the bubble velocity. The increase of A_D is a synergy of bubble rotation and deformation. With the rotation, the angle α between the bubble semi-major axis and the velocity difference $(\boldsymbol{u}-\boldsymbol{v})$ is observed to approximate $\pi/2$, where the expression in Eq. (2.17) achieves the maximum with fixed bubble radius R and aspect ratio d_{31}. And the deformation, namely the rising d_{31}, ensures the steady increase of A_D beyond the

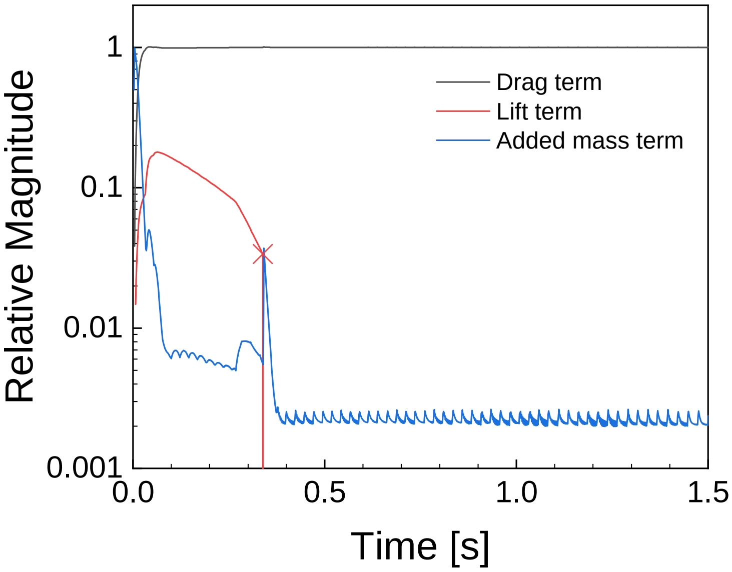

Figure 4.13: The magnitudes of the acceleration terms in motion equation (Eq. 2.12) relative to the magnitude of the constant buoyancy term on a logarithmic scale for $Ca = 0.1$. The red cross highlights the abrupt change of the lift term.

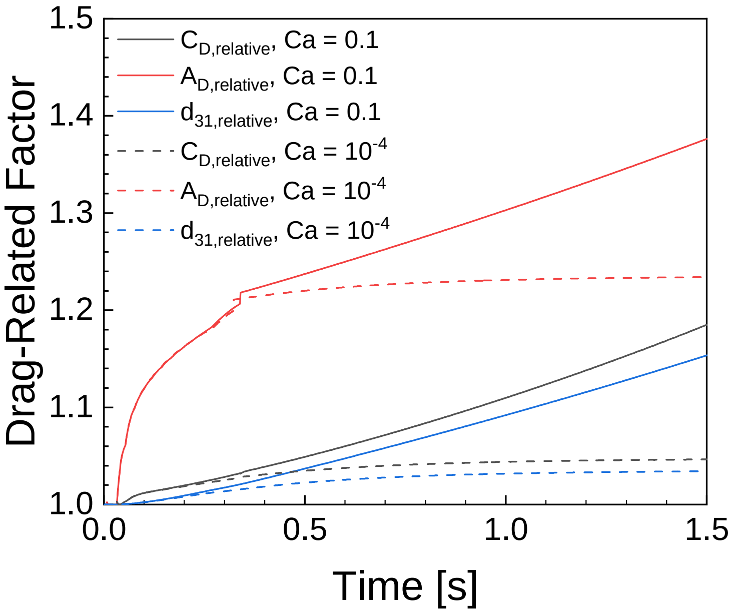

Figure 4.14: Temporal evolution of the drag factor C_D, projected area normal to the direction of drag A_D, and bubble aspect ratio d_{31} relative to their respective reasonable initial value after the initial numerical transience, with $Ca = 0.1$ and 10^{-4}

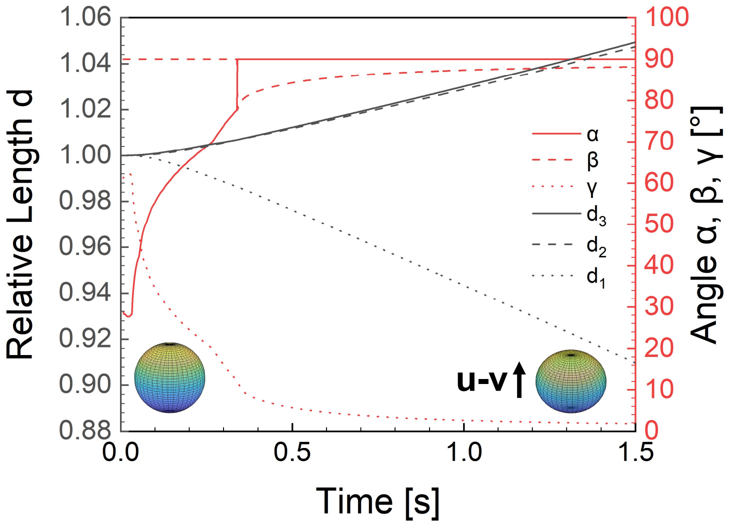

Figure 4.15: Temporal evolutions of the relative lengths of bubble semi-principal axes to their initial values, and the angle between the semi-principal axes and the velocity difference vector $(\boldsymbol{u}-\boldsymbol{v})$ with $Ca = 0.1$. α and d_3 for semi-major axis, γ and d_1 for semi-minor axis, and β and d_2 for the third semi-principal axis.

maximum. Decreasing $(\boldsymbol{u}-\boldsymbol{v})$ due to the growing A_D then lowers the particle Reynold number $Re_p = 2R|\boldsymbol{u}-\boldsymbol{v}|/\nu$, magnifying C_D according to Eq. (2.13). Besides, the drag-related factors showcase a steady state for $Ca = 10^{-4}$, which is in line with its temporal velocity profile in Fig. 4.11.

Moreover, an oblate geometry of the bubble, which is consistent with the experimental observation of Rosenberg [38] and study of Saffman [40], and its tendency to get more oblate is observed throughout the simulation, with the semi-minor axis pointing approximately toward the direction of the bubble motion, as shown in Fig. 4.15. This strategy maximizes the projected area normal to the direction of drag.

These mechanisms together may account for the velocity decrease of the bubble observed in Fig. 4.11 in the two-way coupled case with $Ca = 0.1$, and the general velocity decrease before the steady state of deformable bubbles.

4.3 Decaying isotropic turbulence

4.3.1 Setup and physical quantities

Similar simulation setup as in the work of Grafen is used in this study [15]. To utilize direct numerical simulations (DNS) to investigate the bubble/droplet-laden decaying isotropic

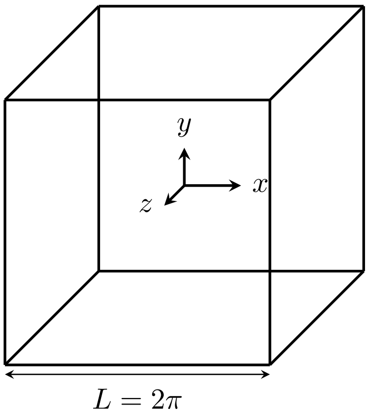

Figure 4.16: Cubic domain for the decaying isotropic turbulence setup with periodic BC at all domain boundaries

$Re^*_{L_b}$	Ma^*	u^*_0	L^*_b	Re^*_λ	κ_p/κ_0	ν^*
2177.5	0.0355	0.020494	256	79.1	4	0.00241

Table 4.1: Initial parameters for decaying isotropic turbulence setup in the LB units

turbulence, an initial condition for single-phase decaying isotropic turbulence was adopted, following the method proposed in references [14, 41]. The configuration for the particle-laden setup was originally suggested by Lucci et al. [23]. The single-phase setup served as a reference state and was compared to the bubble/droplet-laden data. The simulation was carried out in a three-dimensional cubic domain with periodic boundary conditions and a side length of $L = 2\pi$, illustrated in Fig. 4.16.

The initial parameters in Tab. 4.1 are adopted, which are presented in lattice units, analog to the previous studies [14, 15, 41]. $Re^*_{L_b}$ is the Reynolds number concerning the domain length L_b, Ma^* is the Mach number, u^*_0 is the root-mean-square (RMS) velocity, Re^*_λ is the Taylor-scale λ based Reynolds number, κ_p is the peak wave number, $\kappa_0 = 2\pi/L$ is the base wave number, and ν^* is the kinematic viscosity, which is chosen concerning Re^*_λ. According to the Reynolds similarity, $Re^*_\lambda = Re_\lambda = u_0\lambda/\nu$. $\lambda = \lambda_g$ is the transverse Taylor microscale, which can be calculated by

$$\lambda_g = \frac{u_{rms}}{\left\langle \left(\frac{\partial u_i}{\partial x_i}\right)^2 \right\rangle^{\frac{1}{2}}} \tag{4.14}$$

based on the two-point correlation [36], where $\langle \cdot \rangle$ represents a spacially averaged quantity, and $\partial u_i / \partial x_i$ is the velocity partial derivative. The wave number derives from the representation of the fluid velocity field $\boldsymbol{u}$ with the finite Fourier series

$$\boldsymbol{u}(\boldsymbol{x}, t) = \sum_{\boldsymbol{\kappa}} e^{i\boldsymbol{\kappa}\cdot\boldsymbol{x}} \cdot \hat{\boldsymbol{u}}(\boldsymbol{\kappa}, t), \tag{4.15}$$

where the wave number vector $\boldsymbol{\kappa}$ is expressed as $\boldsymbol{\kappa} = \kappa_0(\boldsymbol{e_1} n_1 + \boldsymbol{e_2} n_2 + \boldsymbol{e_3} n_3)$. n_i are integers within the range of $[-N/2+1, N/2]$. The domain consists of $N^3 = (2^8)^3$ spatially discretized cells.

For particle-laden flow configurations, the turbulent kinetic energy budget [42] reads

$$\frac{\partial E_k}{\partial t}(t) = \Psi(t) - \varepsilon(t) = \Psi(t) - \varepsilon_p(t) - \bar{\varepsilon}(t). \tag{4.16}$$

E_k is the turbulent kinetic energy (TKE), a property of the flow field. $\Psi(t)$ is the kinetic energy transfer rate, demonstrating the energy transfer between the flow and the dispersed phase. $\varepsilon(t)$ is the integral viscous dissipation rate, consisting of the particle-induced dissipation rate $\varepsilon_p(t)$, which considers wakes and boundary layers, and the background dissipation rate $\bar{\varepsilon}(t)$, which accounts for the dissipation from the flow itself. According to two-point correlation [36], $\varepsilon(t)$ can be computed by

$$\varepsilon = 15\nu \frac{u_{rms}^2}{\lambda_g^2}. \tag{4.17}$$

Considering the definition of the Kolmogorov length scale η and the Kolmogorov time scale τ_η, which represent the characteristic scales of the smallest eddies, they can be computed by

$$\eta = \sqrt[4]{\frac{\nu^3}{\varepsilon}} \; and \; \tau_\eta = \sqrt{\frac{\nu}{\varepsilon}}. \tag{4.18}$$

The total kinetic energy of the dispersed phase $K(t)$ reads

$$K(t) = \sum_{p=1}^{N_p} \frac{m_p |\boldsymbol{v}_p|^2}{2}, \tag{4.19}$$

where N_p is the number of particles, m_p and $|\boldsymbol{v}_p|$ are the mass and the velocity magnitude of the p-th particle, respectively. The temporal evolution of $K(t)$ can be described by

$$\frac{dK(t)}{dt} = \sum_{p=1}^{N_p} \boldsymbol{F}_p(t) \cdot \boldsymbol{u}_f\left(t, \boldsymbol{x}_p(t)\right) \approx \varepsilon_p(t) - \Psi(t), \tag{4.20}$$

where $\boldsymbol{u}_f$ denotes the undisturbed fluid velocity at the particle position.

Eq. (4.16) can be converted for the wave space by applying Fourier transformation to Eq. (2.1) and Eq. (2.2). The spectral formulation reads

$$\frac{\partial \hat{E}_k}{\partial t}(\boldsymbol{\kappa}, t) = \hat{T}(\boldsymbol{\kappa}, t) + \hat{\Psi}(\boldsymbol{\kappa}, t) - \hat{\varepsilon}(\boldsymbol{\kappa}, t). \tag{4.21}$$

The transfer rate $\hat{T}(\boldsymbol{\kappa}, t)$ expresses the energy transfer between local and non-local wave numbers [36, 41]. With the transformed velocity field $\boldsymbol{u}(\boldsymbol{\kappa})$ according to Eq. (4.15) and force vector $\hat{f}(\boldsymbol{\kappa})$, the other terms can be calculated by

$$\hat{E}_k(\boldsymbol{\kappa}) = \frac{1}{2} \cdot \hat{\boldsymbol{u}}(\boldsymbol{\kappa}) \cdot \hat{\boldsymbol{u}}(\boldsymbol{\kappa}), \tag{4.22}$$

$$\hat{\varepsilon}(\boldsymbol{\kappa}) = 2\mu\boldsymbol{\kappa}^2 \hat{E}_k(\boldsymbol{\kappa}), \tag{4.23}$$

$$\hat{\Psi}(\boldsymbol{\kappa}) = \mathcal{R}\{\hat{\boldsymbol{u}}(\boldsymbol{\kappa}) \cdot \hat{f}(\boldsymbol{\kappa})\}, \tag{4.24}$$

where $\mathcal{R}\{\cdot\}$ represents the real part. These values can be computed for point-particle DNS utilizing wave space integration, which is approximated on discrete wave space through summation (Eq. (4.25)).

$$\Phi(t) = \int_0^\infty \hat{\Phi}(\kappa, t) d\kappa \approx \sum_{\kappa=1}^{\kappa_{\max}} \hat{\Phi}(\kappa, t) \cdot \Delta\kappa \tag{4.25}$$

Φ is an arbitrary quantity, $\Delta\kappa = \kappa_0$, and $\hat{\Phi}(\kappa, t) \cdot \Delta\kappa$ is the contribution to $\Phi(t)$ from the wave number vectors with $|\boldsymbol{\kappa}| \in [j\kappa_0 - \Delta\kappa/2, j\kappa_0 + \Delta\kappa/2]$ [36], $j \in [1, 128]$ for $L_b/2\pi =$ 256 cells.

In the following sections, a non-dimensional timescale $\tilde{t} = \varepsilon_0/u_0^2$ is adopted for the plots, where $\varepsilon_0 = \varepsilon(t=0)$ and $u_0 = u_{rms}(t=0)$ represent the initial viscous dissipation rate and root mean square velocity, respectively. The TKE and viscous dissipation rate are in a non-nondimensional form, relative to $E_{k,0} = E_k(t=0)$ and $\varepsilon_{ref} = u_0^3/L$, respectively. The total kinetic energy of the dispersed phase $K(t)$ is normalized by $K_0 = \phi_m E_{k,0}$, where ϕ_m is the mass fraction of the dispersed phase. A volume fraction $\phi_v = 10^{-3}$ is adopted in all

case	N_p	ρ_p/ρ_c	d/η	d/Δ_{DNS}	ϕ_v	ϕ_m	St_η	Ca
1	45,000	1000	1.758	0.89	10^{-3}	1	172.2	0.1
2	45,000	0.001	1.758	0.89	10^{-3}	10^{-6}	1.722×10^{-4}	0.1

Table 4.2: Initial parameters for studying the influence of the density ratio ρ_p/ρ_c at particle release time $\tilde{t} = 0.26$

the test cases below so that particle collision can be neglected, where a two-way coupling is sufficient [15].

The suitability of the used mesh for a DNS, which calls for accurate resolution of the smallest, dissipative motion with Kolmogorov length scale η, is demonstrated by Grafen [15], where the criterion $\kappa_{\max}\eta \geq 1.5$ [36] is reported to be satisfied. This corresponds to

$$\frac{\eta}{\Delta} \geq \frac{1.5}{\pi} = 0.477, \tag{4.26}$$

where Δ represents the grid spacing. This suitability can be further justified by the temporal evolutions of η/Δ in the test cases below, which demonstrate a global minimum of 0.5.

4.3.2 Influence of the density ratio

The density ratio between the dispersed phase and carrier phase ρ_p/ρ_c is varied to investigate its influence on the behavior of decaying isotropic turbulence, where simulations with parameters in Tab. 4.2 are carried out. The simulation results are demonstrated in Fig. 4.17 ~ Fig. 4.22.

The droplets in case 1 of Tab. 4.2 are observed to correlate with faster decay of TKE and lower level of viscous dissipation, shown in Fig. 4.17, Fig. 4.18, and Fig. 4.20, which is in line with previous studies [15, 41]. The spectral distribution of TKE in the wave number space is decreased by the existence of the droplets below the normalized wave number $\kappa/\kappa_0 \approx 80$ and increased beyond this value. The growth of the Kolmogorov length scale η is accelerated by the distribution of droplets, which is reasonable considering the correlation

$$\eta \propto \varepsilon^{-\frac{1}{4}} \tag{4.27}$$

derived from the definition of η.

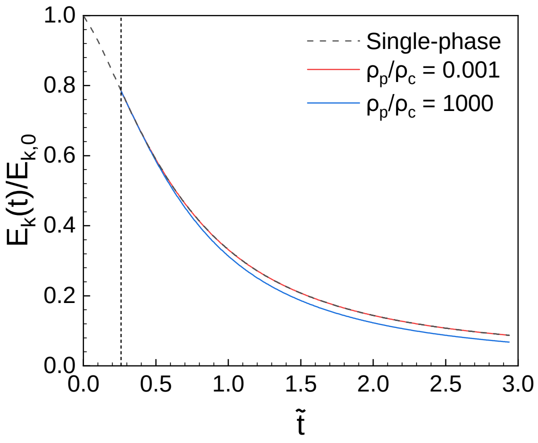

Figure 4.17: Turbulent kinetic energy $E_k(t)$

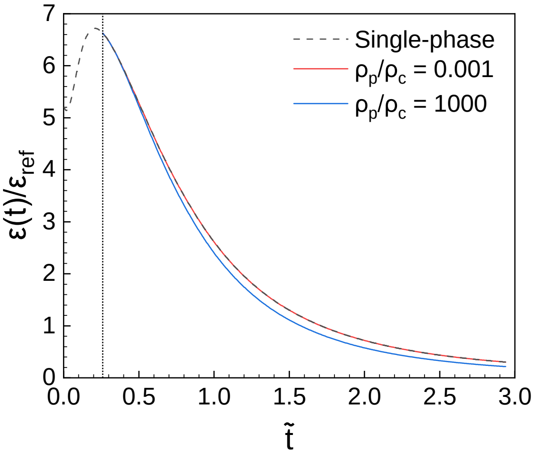

Figure 4.18: Viscous dissipation rate $\varepsilon(t)$

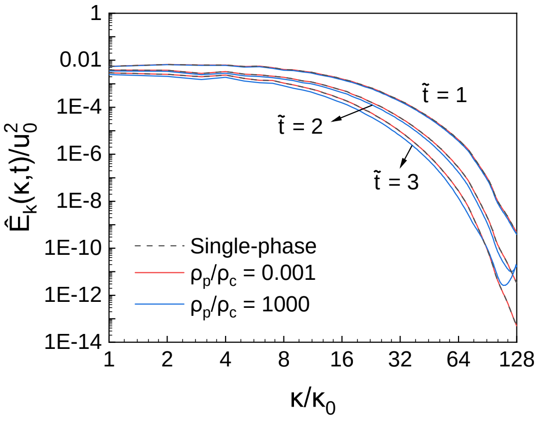

Figure 4.19: Spectral distribution of turbulent kinetic energy $\hat{E}_k(\kappa, t)$

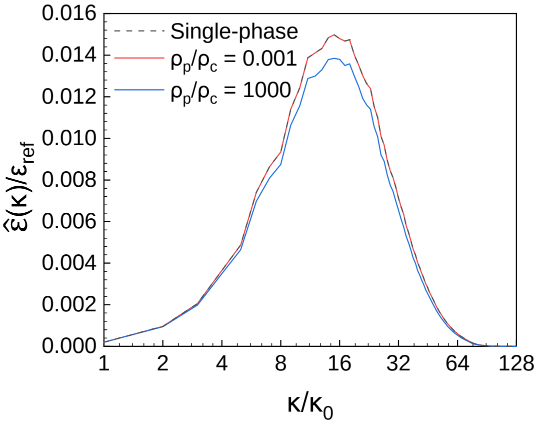

Figure 4.20: Spectral distribution of viscous dissipation rate $\hat{\varepsilon}(\kappa)$ at $\tilde{t} = 1$

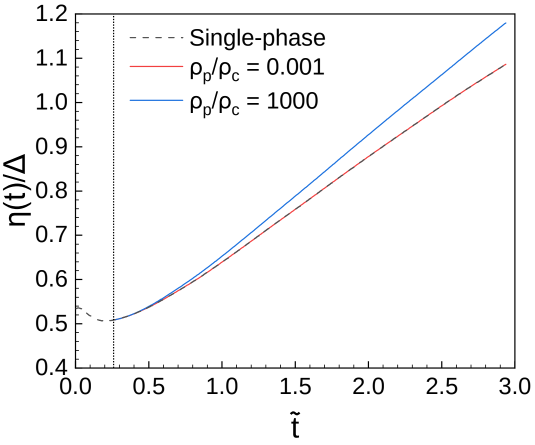

Figure 4.21: Kolmogorov length $\eta(t)/\Delta$

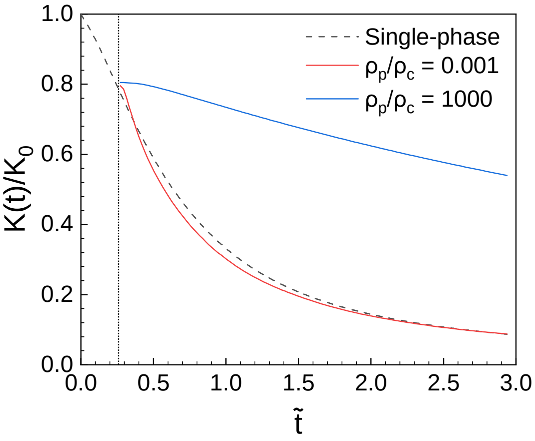

Figure 4.22: Kinetic energy of the dispersed phase $K(t)$

case	N_p	ρ_p/ρ_c	d/η	d/Δ_{DNS}	ϕ_v	ϕ_m	St_η	Ca
1	45,000	1000	1.758	0.89	10^{-3}	1	172.2	0.1
2	45,000	1000	1.758	0.89	10^{-3}	1	172.2	0

Table 4.3: Initial parameters for studying the influence of the capillary number Ca at particle release time $\tilde{t} = 0.26$

The deformable bubbles in case 2 of Tab. 4.2 are observed to hardly affect either the temporal development or the spectral distribution of the integral quantities. In Fig. 4.22, $K(t)$ of droplets deviates far from the single-phase case, while that of bubbles better matches the single-phase scenario. This difference can be attributed to the difference in St_η between the test case 1 and 2. The Stokes number St_η is a non-dimensional number proportional to the particle density, which characterizes the particle inertia. Hence, lower St_η indicates that the motion of the dispersed phase is more vulnerable to the influence of the carrier phase [18]. As bubbles with low St_η are more submissive to the carrier phase, the droplets with higher inertia can better preserve their kinetic energy.

4.3.3 Influence of the capillary number

As the bubbles are observed to barely have an influence on the flow field in the last section, the capillary number Ca is varied for droplets to probe the effect of their deformability on the multiphase system, where simulations with parameters in Tab. 4.3 are carried out. The simulation results are illustrated in Fig. 4.23 $\sim$ Fig. 4.28.

The deformability of the droplets accelerates the decay of TKE and viscous dissipation rate, hence increasing the growth rate of η. So the deformability can be interpreted as a force to push the flow field towards quiescence. This phenomenon may be accounted for by the mechanisms described in Chapter 4.2.2, which illustrates the correlation between bubble deformability and its palliative influence on bubble motion upwards.

The temporal evolution of kinetic energy of the dispersed phase $K(t)$ is slightly decreased after introducing the droplet deformability, despite the same Stokes number St_η. As the droplet's deformation and rotation increase the drag effect, resembling the evolution strategies of the bubble in Chapter 4.2.2, the motion of the dispersed phase may have been better coupled with the carrier phase. So the $K(t)$ curve of deformable droplets lies closer to the single-phase data, which serves as the comparison group.

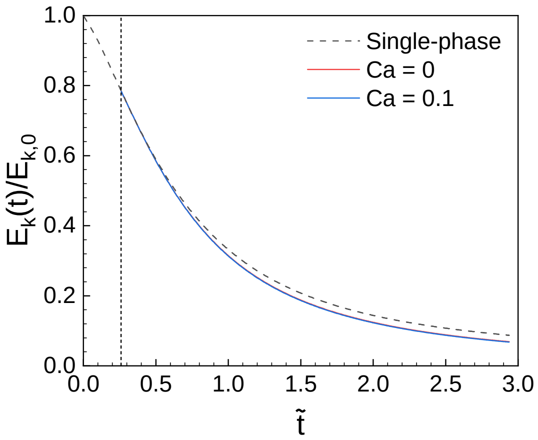

Figure 4.23: Turbulent kinetic energy $E_k(t)$

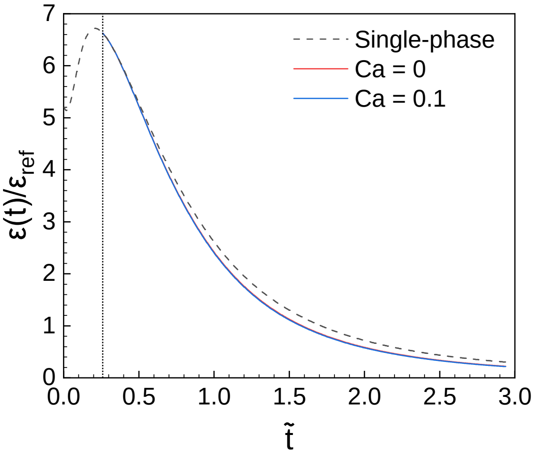

Figure 4.24: Viscous dissipation rate $\varepsilon(t)$

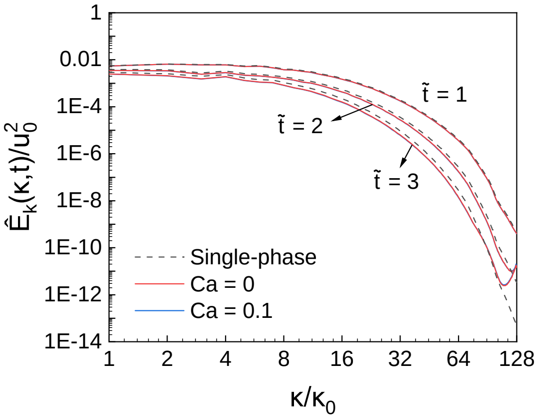

Figure 4.25: Spectral distribution of turbulent kinetic energy $\hat{E}_k(\kappa,t)$

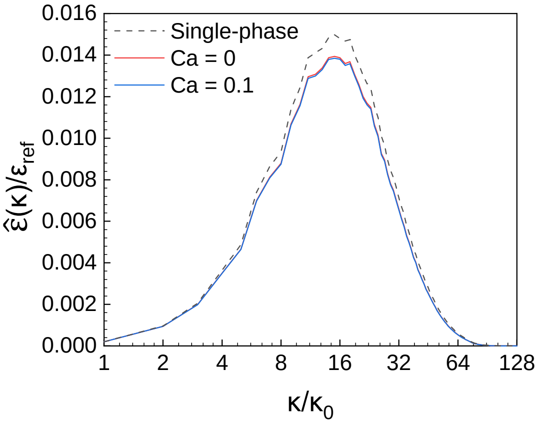

Figure 4.26: Spectral distribution of viscous dissipation rate $\hat{\varepsilon}(\kappa)$ at $\tilde{t} = 1$

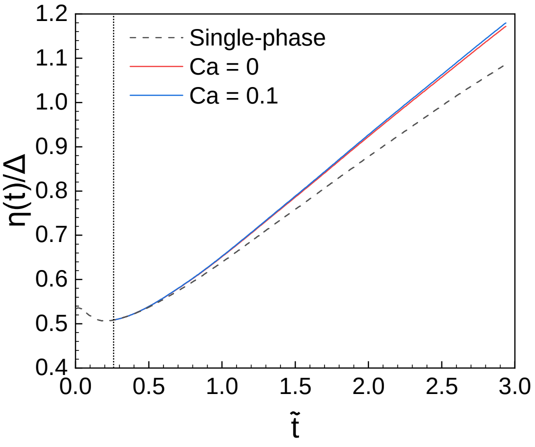

Figure 4.27: Kolmogorov length $\eta(t)/\Delta$

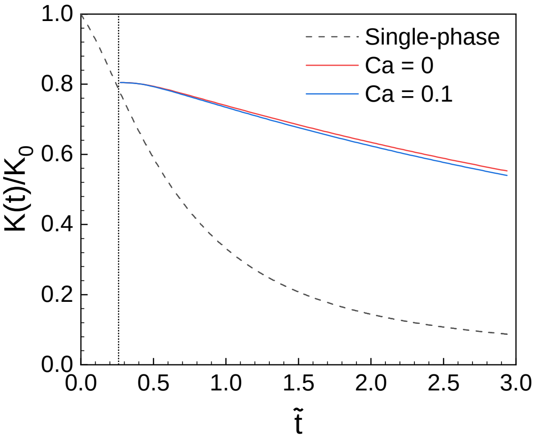

Figure 4.28: Kinetic energy of the dispersed phase $K(t)$

case	N_p	ρ_p/ρ_c	d/η	d/Δ_{DNS}	ϕ_v	ϕ_m	St_η	Ca
1	45,000	1000	1.758	0.89	10^{-3}	1	172.2	0.1
2	10,000	1000	2.903	1.47	10^{-3}	1	469.5	0.1
3	45,000	0.001	1.758	0.89	10^{-3}	10^{-6}	1.722×10^{-4}	0.1
4	100,000	0.001	1.347	0.68	10^{-3}	10^{-6}	1.011×10^{-4}	0.1

Table 4.4: Initial parameters for studying the influence of bubble/droplet diameter d at particle release time $\tilde{t} = 0.26$

4.3.4 Influence of bubble/droplet diameter

Finally, the droplet and bubble diameter is varied, keeping the volume fraction constant. The simulations with parameters in Tab. 4.4 are carried out, and the results of droplets are juxtaposed in Fig. 4.29 $\sim$ Fig. 4.34, those of bubbles in Fig. 4.35 $\sim$ Fig. 4.40.

Smaller droplets, corresponding to larger droplet quantity, are observed to accelerate the decay of TKE and viscous dissipation rate and increase the growth rate of η. Larger droplets better preserve their kinetic energy due to their larger inertia, demonstrated in Fig. 4.34.

The influence of the bubbles on the TKE, viscous dissipation rate, and η of the fluid is negligible, shown in Fig. 4.35 $\sim$ Fig. 4.39. And the bubbles with smaller inertia, which is case 4, are observed to demonstrate a $K(t)$ more resembles the temporal evolution pattern of TKE of the single-phase comparison group, illustrated in Fig. 4.40, which is in line with the deduction in previous subsections.

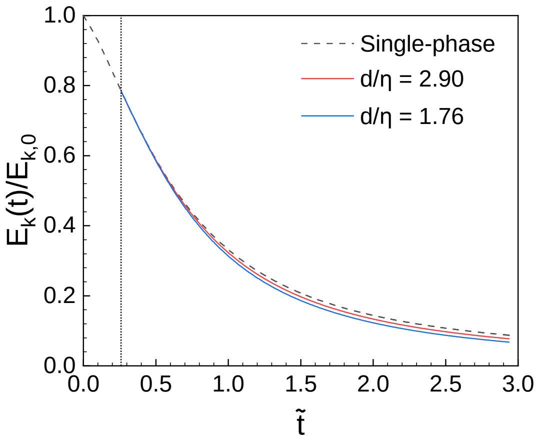

Figure 4.29: Turbulent kinetic energy $E_k(t)$

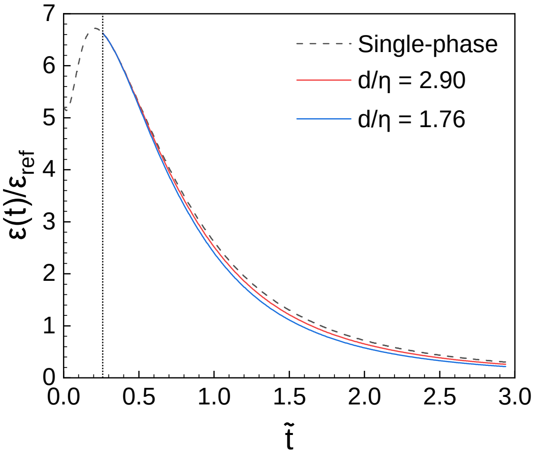

Figure 4.30: Viscous dissipation rate $\varepsilon(t)$

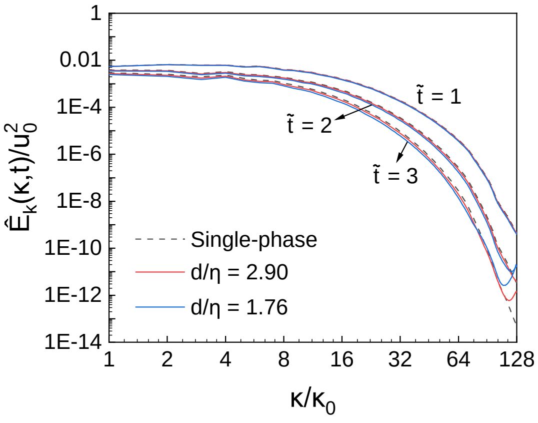

Figure 4.31: Spectral distribution of turbulent kinetic energy $\hat{E}_k(\kappa, t)$

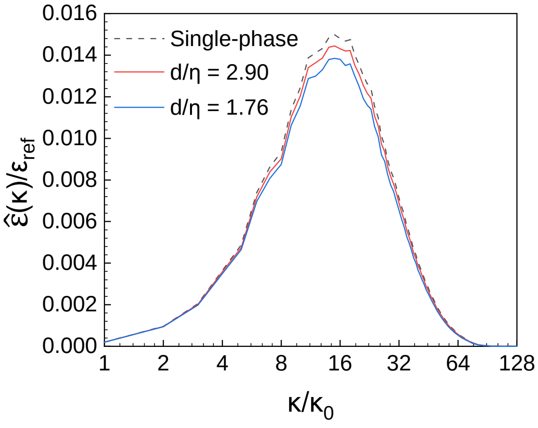

Figure 4.32: Spectral distribution of viscous dissipation rate $\hat{\varepsilon}(\kappa)$ at $\tilde{t} = 1$

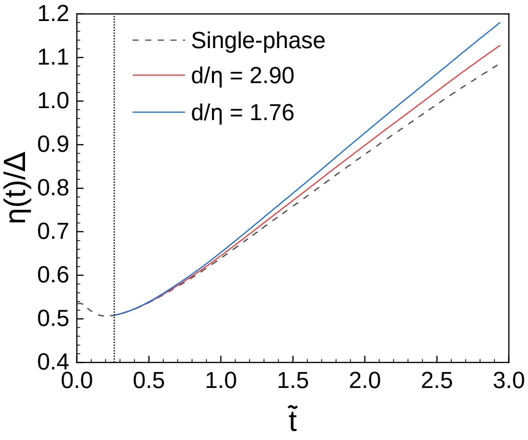

Figure 4.33: Kolmogorov length $\eta(t)/\Delta$

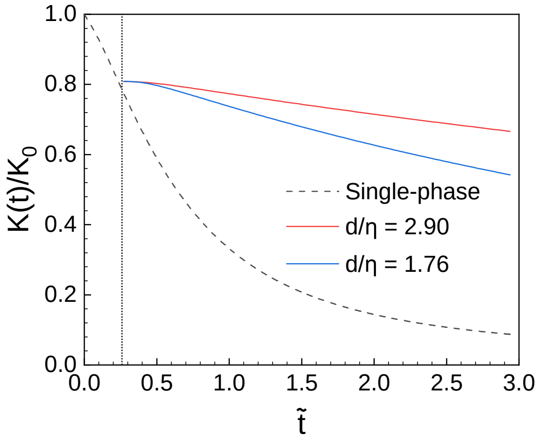

Figure 4.34: Kinetic energy of the dispersed phase $K(t)$

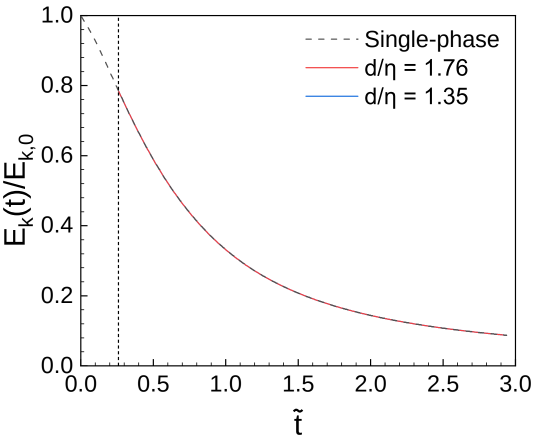

Figure 4.35: Turbulent kinetic energy $E_k(t)$

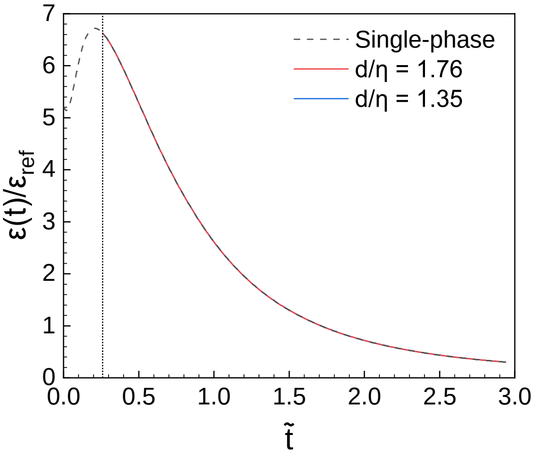

Figure 4.36: Viscous dissipation rate $\varepsilon(t)$

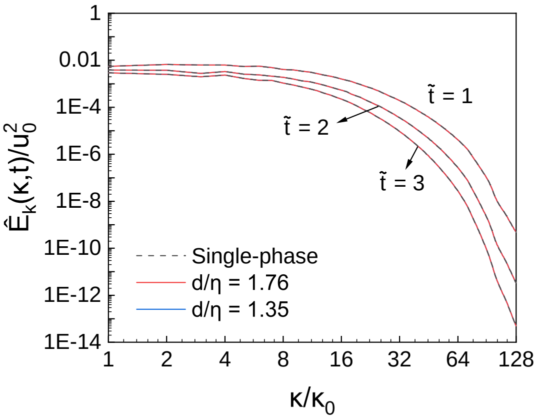

Figure 4.37: Spectral distribution of turbulent kinetic energy $\hat{E}_k(\kappa, t)$

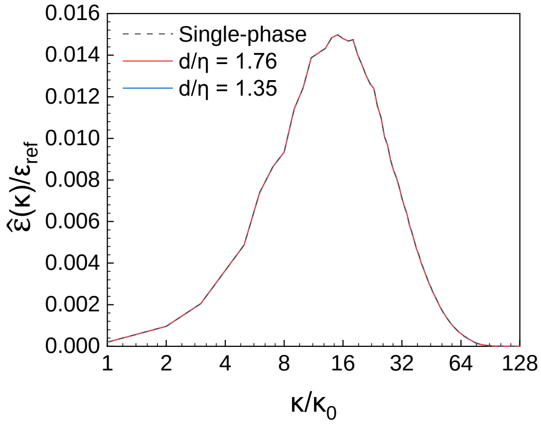

Figure 4.38: Spectral distribution of viscous dissipation rate $\hat{\varepsilon}(\kappa)$ at $\tilde{t} = 1$

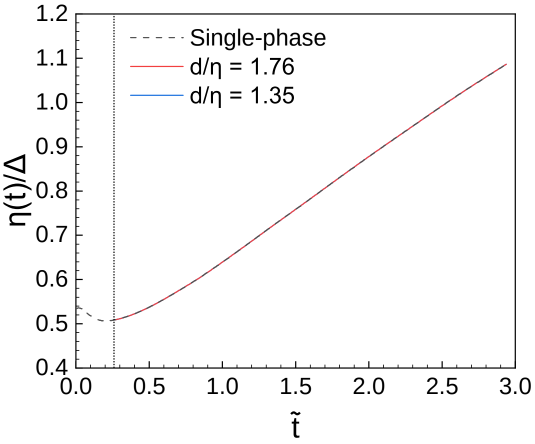

Figure 4.39: Kolmogorov length $\eta(t)/\Delta$

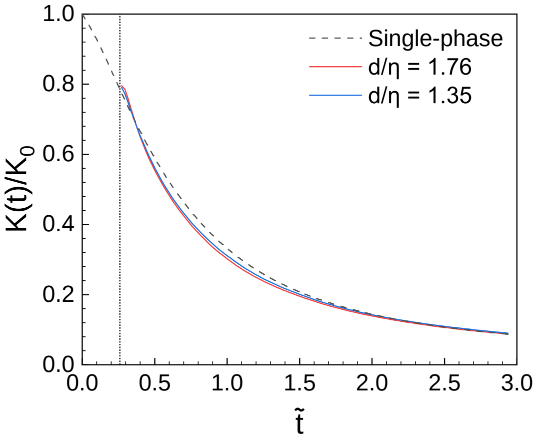

Figure 4.40: Kinetic energy of the dispersed phase $K(t)$

5

Summary and Outlook

In this thesis, the Lagrangian Particle Tracking (LPT) solver of the in-house fluid flow solver m-AIA was extended for the case of deformable Kolmogorov-sized bubbles and droplets. The shape function proposed by Maffettone and Minale [24] was implemented to account for the morphological evolution of the bubbles and droplets, where extra volume and shape correction steps are added to compensate for the discretization error. The motion equation formulated by Yin et al. [55] and Njobuenwu et al. [33], which was adopted by Spadan et al. [45] in their study of sub-Kolmogorov deformable bubbles, was implemented to consider the dynamics of axisymmetrical ellipsoids.

For the validation purpose, the morphological evolution of a single bubble/droplet is examined in the test cases of relaxation, shear flow, and vortex. The eigenvalues of the shape function demonstrate quasi-exponential decay in the relaxation test case, where the temporal evolution of the time constant is in line with the theoretical deduction. The particle steady-state orientation and aspect ratio in the shear flow test case are in line with the analytical prediction [24] and experimentally justified results [16, 37, 39]. Moreover, the analytical model is extended to investigate the morphological behavior of the bubble/droplet in the scenarios between shear flow and vortex. The linear rotational behavior is demonstrated in the vortex test case, where the correction step nullifies the rotation-induced geometrical error. Perfect volume conservation is evidenced in all three test cases above.

The motion equation is validated in the rising bubble test case with coupling between the LPT solver and Lattice Boltzmann method (LBM) solver, where the bubble velocity magnitude in the one-way coupled test case perfectly dwells in the calculated analytical terminal velocity. The two-way coupling was observed to slightly increase the bubble terminal velocity, and the rising bubble deformability palliates the bubble motion by increasing the oblateness. Both bubble rotation and deformation are observed to account for the smaller terminal velocity than the rigid case.

Finally, studies of bubble/droplet-laden decaying isotropic turbulence DNS using the LBM-LPT two-way coupling algorithm were conducted. The influence of the density ratio between the dispersed phase and carrier phase, droplet deformability, and particle diameter on the flow field and the dispersed phase are investigated. The bubbles are observed to barely affect the flow field. Larger droplet deformability and smaller diameter are found to accelerate the decay of the turbulence. And the droplet deformability is speculated to improve the coupling between the dispersed phase and carrier phase by enhancing the drag effect.

Since inter-particle collisions are yet to be implemented, the current simulation module is limited to the two-way coupling regime, where the volume fraction of the dispersed phase is below 10^{-3}. Besides, the wall-collision model is yet to be built for the simulation of Taylor-Couette flow. Moreover, the current version of the motion equation does not apply to deformable bubbles/droplets with capillary numbers $Ca \geq 0.1$. Hence, the dynamics in the region between $Ca = 0.1$ and the theoretical maximum $Ca = 0.58 \pm 0.05$ [24] or the simulated rupture limit $Ca = 0.286 \pm 0.006$ [29] has so far been impermeable. Proper formulation of the motion equation is yet to be found to account for this region. These circumstances may be accounted for in future efforts.

References

[1] Acheson, D. (1990). *Elementary fluid dynamics*. Clarendon Press.

[2] Batchelor, C.K. (2010). *An introduction to fluid dynamics*. Cambridge mathematical library, Cambridge University Press, Cambridge, 14th edn.

[3] Bhatnagar, P.L., Gross, E.P. & Krook, M. (1954). A model for collision processes in gases. i. small amplitude processes in charged and neutral one-component systems. *Physical Review*, **94**, 511–525.

[4] Biferale, L., Meneveau, C. & Verzicco, R. (2014). Deformation statistics of sub-kolmogorov-scale ellipsoidal neutrally buoyant drops in isotropic turbulence. *Journal of Fluid Mechanics*, **754**, 184–207.

[5] Chen, S. & Doolen, G.D. (1998). Lattice boltzmann method for fluid flows. *Annual Review of Fluid Mechanics*, **30**, 329–364.

[6] Chouippe, A., Climent, E., Legendre, D. & Gabillet, C. (2014). Numerical simulation of bubble dispersion in turbulent taylor-couette flow. *Physics of Fluids*, **26**.

[7] Clift, R., Grace, J.R. & Weber, M.E. (2013). *Bubbles, drops, and particles*. Dover Publ, Mineola, NY.

[8] Crowe, C.T. (2012). *Multiphase flows with droplets and particles*. CRC Press, Boca Raton, FL, 2nd edn.

[9] Dabiri, S. & Tryggvason, G. (2015). Heat transfer in turbulent bubbly flow in vertical channels. *Chemical Engineering Science*, **122**, 106–113.

[10] Duduković, M.P., Larachi, F. & Mills, P.L. (2002). Multiphase catalytic reactors: a perspective on current knowledge and future trends. *Catalysis Reviews*, **44**, 123–246.

[11] ELLINGSEN, K. & Risso, F. (2001). On the rise of an ellipsoidal bubble in water: oscillatory paths and liquid-induced velocity. *Journal of Fluid Mechanics*, **440**, 235–268.

[12] Ern, P., Risso, F., Fabre, D. & Magnaudet, J. (2012). Wake-induced oscillatory paths of bodies freely rising or falling in fluids. *Annual Review of Fluid Mechanics*, **44**, 97–121.

[13] Ganser, G.H. (1993). A rational approach to drag prediction of spherical and nonspherical particles. *Powder Technology*, **77**, 143–152.

[14] Gao, H., Li, H. & Wang, L.P. (2013). Lattice boltzmann simulation of turbulent flow laden with finite-size particles. *Computers & Mathematics with Applications*, **65**, 194–210.

[15] Grafen, J.L. (2022). Two-way coupling of a lagrangian point-particle model with a lattice boltzmann method.

[16] Hinch, E.J. & Acrivos, A. (1980). Long slender drops in a simple shear flow. *Journal of Fluid Mechanics*, **98**, 305–328.

[17] Hoerner, S.F. (1965). *Fluid-dynamic drag: Practical information on aerodynamic drag and hydrodynamic resistance*. Hoerner Fluid Dynamics, Bakersfield, 2nd edn.

[18] Krstić, M. (2006). Chapter 9 - mixing control for jet flows. In G.D. Roy, ed., *Combustion processes in propulsion*, 87–96, Elsevier Butterworth-Heinemann, Amsterdam and London.

[19] Krüger, T., Kusumaatmaja, H., Kuzmin, A., Shardt, O., Silva, G. & Viggen, E.M. (2016). *The lattice Boltzmann method: Principles and practice / Timm Krüger, Halim Kusumaatmaja, Alexandr Kuzmin, Orest Shardt, Goncalo Silva, Erlend Magnus Viggen*. Graduate texts in physics, 1868-4513, Springer, Switzerland, 1st edn.

[20] Lai, R.Y.S. & Mockros, L.F. (1972). The stokes-flow drag on prolate and oblate spheroids during axial translatory accelerations. *Journal of Fluid Mechanics*, **52**, 1–15.

[21] Lu, J. & Tryggvason, G. (2008). Effect of bubble deformability in turbulent bubbly upflow in a vertical channel. *Physics of Fluids*, **20**.

[22] Lu, J., Fernández, A. & Tryggvason, G. (2005). The effect of bubbles on the wall drag in a turbulent channel flow. *Physics of Fluids*, **17**.

[23] LUCCI, F., FERRANTE, A. & ELGHOBASHI, S. (2010). Modulation of isotropic turbulence by particles of taylor length-scale size. *Journal of Fluid Mechanics*, **650**, 5–55.

[24] Maffettone, P.L. & Minale, M. (1998). Equation of change for ellipsoidal drops in viscous flow. *Journal of Non-Newtonian Fluid Mechanics*, **78**, 227–241.

[25] Magnaudet, J. & Eames, I. (2000). The motion of high-reynolds-number bubbles in inhomogeneous flows. *Annual Review of Fluid Mechanics*, **32**, 659–708.

[26] Marchioli, C., Fantoni, M. & Soldati, A. (2010). Orientation, distribution, and deposition of elongated, inertial fibers in turbulent channel flow. *Physics of Fluids*, **22**.

[27] Maxey, M.R. (1983). Equation of motion for a small rigid sphere in a nonuniform flow. *Physics of Fluids*, **26**, 883.

[28] Mazzitelli, I.M., Lohse, D. & Toschi, F. (2003). The effect of microbubbles on developed turbulence. *Physics of Fluids*, **15**, L5–L8.

[29] Milan, F., Biferale, L., Sbragaglia, M. & Toschi, F. (2020). Sub-kolmogorov droplet dynamics in isotropic turbulence using a multiscale lattice boltzmann scheme. *Journal of Computational Science*, **45**.

[30] Minale, M. (2008). A phenomenological model for wall effects on the deformation of an ellipsoidal drop in viscous flow. *Rheologica Acta*, **47**, 667–675.

[31] Minale, M. (2010). Models for the deformation of a single ellipsoidal drop: a review. *Rheologica Acta*, **49**, 789–806.

[32] Mougin, G. & Magnaudet, J. (2002). Path instability of a rising bubble. *Physical Review Letters*, **88**.

[33] Njobuenwu, D.O. & Fairweather, M. (2015). Dynamics of single, non-spherical ellipsoidal particles in a turbulent channel flow. *Chemical Engineering Science*, **123**, 265–282.

[34] Olmos, E., Gentric, C., Vial, C., Wild, G. & Midoux, N. (2001). Numerical simulation of multiphase flow in bubble column reactors. influence of bubble coalescence and break-up. *Chemical Engineering Science*, **56**, 6359–6365.

[35] Olsen, J.E. & Skjetne, P. (2016). Modelling of underwater bubble plumes and gas dissolution with an eulerian-lagrangian cfd model. *Applied Ocean Research*, **59**, 193–200.

[36] Pope, S.B. (2000). *Turbulent flows*. Cambridge University Press, Cambridge.

[37] Rallison, J.M. (1980). Note on the time-dependent deformation of a viscous drop which is almost spherical. *Journal of Fluid Mechanics*, **98**, 625.

[38] Rosenberg, B. & David W. Taylor Model Basin. (1950). *The Drag and shape of air bubbles moving in liquids*, vol. 727 of *Report*. Navy Dept., David W. Taylor Model Basin, Washington, D.C.

[39] Rust, A.C. & Manga, M. (2002). Bubble shapes and orientations in low re simple shear flow. *Journal of Colloid and Interface Science*, **249**, 476–480.

[40] Saffman, P.G. (1956). On the rise of small air bubbles in water. *Journal of Fluid Mechanics*, **1**, 249–275.

[41] Schneiders, L. (2017). *Particle-Resolved Analysis of Turbulent Multiphase Flow by a Cut-Cell Method*. Dissertation, Rheinisch-Westfälische Technische Hochschule Aachen, München.

[42] Schneiders, L., Meinke, M. & Schröder, W. (2017). Direct particle–fluid simulation of kolmogorov-length-scale size particles in decaying isotropic turbulence. *Journal of Fluid Mechanics*, **819**, 188–227.

[43] Silva, G. & Semiao, V. (2014). Truncation errors and the rotational invariance of three-dimensional lattice models in the lattice boltzmann method. *Journal of Computational Physics*, **269**, 259–279.

[44] Spandan, V., Lohse, D. & Verzicco, R. (2016). Deformation and orientation statistics of neutrally buoyant sub-kolmogorov ellipsoidal droplets in turbulent taylor–couette flow. *Journal of Fluid Mechanics*, **809**, 480–501.

[45] Spandan, V., Verzicco, R. & Lohse, D. (2017). Deformable ellipsoidal bubbles in taylor-couette flow with enhanced euler-lagrangian tracking. *Physical Review Fluids*, **2**.

[46] SUGIYAMA, K., CALZAVARINI, E. & Lohse, D. (2008). Microbubbly drag reduction in taylor–couette flow in the wavy vortex regime. *Journal of Fluid Mechanics*, **608**, 21–41.

[47] Terasaka, K., Hirabayashi, A., Nishino, T., Fujioka, S. & Kobayashi, D. (2011). Development of microbubble aerator for waste water treatment using aerobic activated sludge. *Chemical Engineering Science*, **66**, 3172–3179.

[48] Tryggvason, G., Bunner, B., Esmaeeli, A., Juric, D., Al-Rawahi, N., Tauber, W., Han, J., Nas, S. & Jan, Y.J. (2001). A front-tracking method for the computations of multiphase flow. *Journal of Computational Physics*, **169**, 708–759.

[49] Unverdi, S.O. & Tryggvason, G. (1992). A front-tracking method for viscous, incompressible, multi-fluid flows. *Journal of Computational Physics*, **100**, 25–37.

[50] van Gils, D.P.M., Narezo Guzman, D., Sun, C. & Lohse, D. (2013). The importance of bubble deformability for strong drag reduction in bubbly turbulent taylor–couette flow. *Journal of Fluid Mechanics*, **722**, 317–347.

[51] Vananroye, A., van Puyvelde, P. & Moldenaers, P. (2011). Deformation and orientation of single droplets during shear flow: combined effects of confinement and compatibilization. *Rheologica Acta*, **50**, 231–242.

[52] Verschoof, R.A., van der Veen, R.C.A., Sun, C. & Lohse, D. (2016). Bubble drag reduction requires large bubbles. *Physical Review Letters*, **117**.

[53] Voth, G.A. & Soldati, A. (2017). Anisotropic particles in turbulence. *Annual Review of Fluid Mechanics*, **49**, 249–276.

[54] Wang, S., Zhang, A., Liu, Y. & Zeng, D. (2013). Numerical simulation of bubble dynamics in an elastic vessel. *The European Physical Journal E*, **36**, 119.

[55] Yin, C., Rosendahl, L., Knudsen Kær, S. & Sørensen, H. (2003). Modelling the motion of cylindrical particles in a nonuniform flow. *Chemical Engineering Science*, **58**, 3489–3498.

[56] Zhang, H., Ahmadi, G., Fan, F.G. & McLaughlin, J.B. (2001). Ellipsoidal particles transport and deposition in turbulent channel flows. *International Journal of Multiphase Flow*, **27**, 971–1009.

Declaration

I herewith declare that the present thesis is the result of my own work without the prohibited assistance of third parties and without making use of aids other than those specified; it includes nothing which is the outcome of work done by other authors, unless for commonly understood ideas or where identified to the contrary. This thesis has not previously been presented in identical or similar form to any other institution, German or foreign, for any degree or any other qualification.

Aachen, 27th April 2023